

Upcycling spent medium-Ni cathodes *via* novel liquified salt sourcing†

Cite this: DOI: 10.1039/d5ee01086a

Moonsu Yoon,^{id} ^{ab} Jin-Sung Park,^{acd} Weiyin Chen,^a Yimeng Huang,^a Tao Dai,^a Yumin Lee,^b Jungmin Shin,^b Seungmi Lee,^b Yongil Kim,^{id} ^b Dongsoo Lee,^b Daiha Shin,^e Jaephil Cho,^{id} ^f Yanhao Dong^{id} *^g and Ju Li^{id} *^{ah}

The rapid growth in lithium-ion battery technology underscores the urgent need for sustainable recycling to address the environmental and economic challenges of battery waste. This study introduces a liquified-salts-assisted upcycling approach to transform spent medium-Ni cathodes into high-performance single-crystalline Ni-rich cathodes. Utilizing the LiOH–LiNO₃–Ni(NO₃)₂·6H₂O eutectic, this method leverages planetary centrifugal mixing to create a liquid-like environment for accelerated elemental diffusion and microstructural refinement. The *in situ* liquefaction of these salts ensures seamless precursor integration, achieving compositional uniformity and minimizing impurity formation. Compared to conventional solid-state methods, our method significantly suppresses rock-salt phase formation, and improves electrochemical performance with superior cycling stability and rate capability. The environmental and economic advantages of our approach highlight its potential to reduce greenhouse gas emissions and energy consumption. This scalable, energy-efficient strategy provides a transformative solution for battery waste management, paving the way for the sustainable production of next-generation cathode materials.

Received 24th February 2025,
Accepted 2nd April 2025

DOI: 10.1039/d5ee01086a

rsc.li/ees

Broader context

The rapid expansion of lithium-ion battery usage, driven by electric vehicles and renewable energy storage, has raised significant environmental and economic concerns regarding the management of end-of-life batteries. Traditional recycling methods, such as hydrometallurgy and pyrometallurgy, often involve environmentally harmful processes, high energy consumption, and substantial waste generation. This research introduces a novel liquified-salts-assisted upcycling strategy for transforming spent medium-nickel cathodes into high-performance, Ni-rich cathode materials. By utilizing a eutectic mixture of LiOH–LiNO₃ and Ni(NO₃)₂·6H₂O, combined with planetary centrifugal mixing, this method significantly reduces energy consumption, minimizes greenhouse gas emissions, and achieves superior electrochemical performance compared to conventional recycling techniques. This scalable and sustainable approach addresses critical environmental issues associated with battery waste and provides a practical pathway toward the circular economy, supporting the sustainable growth of next-generation battery technologies.

Introduction

The growing global demand for carbon-neutral energy has made lithium-ion batteries (LIBs) indispensable for large-scale energy storage, particularly in applications such as

electric vehicles and grid systems.^{1–3} The market for rechargeable LIBs was valued at approximately \$46 billion in 2022, and is projected to reach \$190 billion by 2032, growing at an annual rate of nearly 15%.^{4,5} With a typical lifespan of less than 10 years, the foreseeable staggering accumulation of

^a Department of Nuclear Science and Engineering, Massachusetts Institute of Technology, Cambridge, Massachusetts, 02139, USA. E-mail: liju@mit.edu^b Department of Chemical, Biological and Battery Engineering, Gachon University, Seongnam, 13120, Republic of Korea^c Department of Materials Science and Engineering, Ajou University, Suwon, 16499, Republic of Korea^d Department of Energy Systems Research, Ajou University, Suwon, 16499, Republic of Korea^e Metropolitan Seoul Center, Korea Basic Science Institute, Seoul, 03759, Republic of Korea^f Department of Energy Engineering, School of Energy and Chemical Engineering, Ulsan National Institute of Science and Technology, Ulsan, 44919, Republic of Korea^g State Key Laboratory of New Ceramics and Fine Processing, School of Materials Science and Engineering, Tsinghua University, Beijing, 100084, China.

E-mail: dongyanhao@tsinghua.edu.cn

^h Department of Material Science and Engineering, Massachusetts Institute of Technology, Cambridge, Massachusetts, 02139, USA† Electronic supplementary information (ESI) available. See DOI: <https://doi.org/10.1039/d5ee01086a>

spent/degraded LIBs raises significant concerns about sustainability. There is an urgent need for advanced recycling technologies and infrastructure to manage such waste.^{6,7} The primary focus in spent LIB recycling is on cathode materials, which constitute more than one-third of the LIB total weight and nearly half of its cost.^{8,9} In particular, high-value metallic elements (Ni, Co, and Li), in ternary cathode materials NCM ($\text{LiNi}_x\text{Co}_y\text{Mn}_z\text{O}_2$, $x + y + z = 1$), are unevenly distributed globally, imposing significant environmental and social burdens for mining and transportation.^{10–13} Effective closed-loop recycling strategies are essential to mitigate the environmental impact of battery wastes and reduce reliance on resource-intensive mining practices.

As a cutting-edge method, “upcycling” has emerged to offset the recycling cost by ensuring higher value and superior performance. Direct conversion from Ni-lean to higher-energy-density Ni-rich compositions is gaining significant attention, as medium-Ni NCM with $x \leq 0.5$ were the first ones mass-produced and will be the first ones to retire among the ternary cathode family.^{14–16} One of the most practiced upcycling approaches is *via* hydrometallurgy, which reclaims the simple metals, oxides, or their salts from the spent cathode materials.^{17–19} It typically involves destroying the entire cathode microstructure in acidic leaching solutions at mild temperatures, enabling the recovery of valuable metal elements (including Li) in the form of salt precursors (*e.g.*, Li_2CO_3 and $\text{M}(\text{SO}_4)_x \cdot x\text{H}_2\text{O}$, $\text{M} = \text{Ni}, \text{Co}, \text{and Mn}$). However, a massive amount of wastewater is inevitably generated during the neutralization process of the strong acid solutions, which continues to raise environmental and safety concerns. Alternatively, the pyrometallurgical method, the most widely used approach in the field of heavy industry, can recover metal (Ni, Co, and Mn) alloys through high-temperature ($> 1200\text{--}1600\text{ }^\circ\text{C}$) smelting and refining.^{20,21} However, it must undergo complex steps to convert the alloys into high-purity Ni-rich precursor with micron-sized morphology. Furthermore, the destructive recycling methods of both hydrometallurgy and pyrometallurgy limit their output to lower-value products (such as salt precursors or alloys) derived from spent cathodes. Therefore, energy-consuming resynthesis steps are still required to recreate the high-value NCM cathodes with optimal stoichiometry and crystal structure.^{22,23}

Direct upcycling offers a non-destructive alternative by utilizing spent cathode powders as precursors in the subsequent resynthesis of cathodes.^{24–26} By supplying the lost Li and additional Ni to the spent Ni-lean cathodes, Ni-rich cathode materials can be directly synthesized to build new LIBs. Despite requiring pre-treatment steps, such as the removal of organic residues (electrolytes, carbon additives, and binders) and quantification of Li deficiency, direct upcycling has distinct economic and environmental advantages over hydrometallurgy and pyrometallurgy approaches.²⁵ In the domain of direct upcycling, the solid-state synthesis method is particularly noteworthy for its simplicity and compatibility with the conventional manufacturing process for TM-based (*e.g.* layered/spinel/olivine-types) cathode materials (Fig. 1). This method typically entails mechanically mixing a Li source (*e.g.*, LiOH) and a Ni source (*e.g.*, NiO or $\text{Ni}(\text{OH})_2$) with the spent Ni-lean (or medium-Ni) cathode powders, followed by high-temperature

calcination ($> 800\text{ }^\circ\text{C}$). However, solid-state synthesis faces inherent limitations in achieving uniform contact between the solid precursors.²⁷ Mechanical mixing often necessitates prolonged high-energy ball-milling (sometimes lasting hundreds of hours at thousands of rounds per minute), to deagglomerate the micro-sized secondary particles into nano-sized particles,^{15,28,29} ensuring a more even contact between various precursors and spent cathode particles (Fig. 1). Without such energy-intensive preparation, diffusion pathways for Li and Ni during sintering remain restricted, often leading to the formation of impurity phases, such as Ni-rich rock-salt and residual Li compounds on the cathode surface. These impurities potentially degrade the electrochemical performance of re-synthesized Ni-rich cathodes. More importantly, the reliance on high-energy ball-milling poses a significant barrier to scaling up solid-state upcycling methods beyond the laboratory scale.^{30,31} Given the challenges and limited industrial viability of the current direct upcycling method, developing a simple and scalable strategy is crucial to managing the upcoming end-of-life of widely employed LIBs.

Herein, we propose a novel liquified-salt-assisted upcycling approach that overcomes the limitations of conventional direct recycling and upcycling methods (Fig. 1). This strategy utilizes a eutectic mixture of LiOH–LiNO₃ along with $\text{Ni}(\text{NO}_3)_2 \cdot 6\text{H}_2\text{O}$ to accelerate the liquefaction and dispersion of precursor salts and spent cathode particles, creating a liquid-like environment during planetary centrifugal mixing. The *in situ* melting of eutectic Li-salts and liquified nitrates promotes rapid dissolution and dispersion, and provides a seamless integration of elemental replenishment and microstructural refinement, thus enabling the transformation of spent medium-Ni cathodes into high-performance Ni-rich cathodes with single-crystalline morphology. Beyond its environmental and economic advantages, this scalable and energy-efficient technique redefines the potential of upcycling, paving the way for sustainable LIB waste management and the development of next-generation high-energy-density cathode materials.

Results and discussion

Ni-enriched precursors sourced from waste cathodes and eutectic liquified salts

We chose a spent $\text{LiNi}_{0.5}\text{Co}_{0.2}\text{Mn}_{0.3}\text{O}_2$ (NCM523) cathode as the precursors for upcycling due to its prominence as a commercial cathode material in the past decade. Following mild heat treatment ($\sim 400\text{ }^\circ\text{C}$, 20 min) and manual scraping, we separated and collected the spent NCM523 powders (Li deficient, with chemical formula $\text{Li}_x\text{Ni}_{0.5}\text{Co}_{0.2}\text{Mn}_{0.3}\text{O}_2$ and $x \approx 0.8$) from cathode electrodes, as detailed in Fig. S1 and S2 (ESI[†]). To demonstrate the liquified-salts-assisted upcycling method, we employed a planetary centrifugal mixer (THINKY ARE-310, maximum capacity: $\sim 310\text{ g}$)—a device commonly used for mixing, dispersing, deaerating and slurry preparation—in the present study. Targeting a Ni-rich layered cathode $\text{Li}_{1.0}\text{Ni}_{0.80}\text{Co}_{0.08}\text{Co}_{0.12}\text{O}_2$ (NCM811) as the final product, we mixed spent



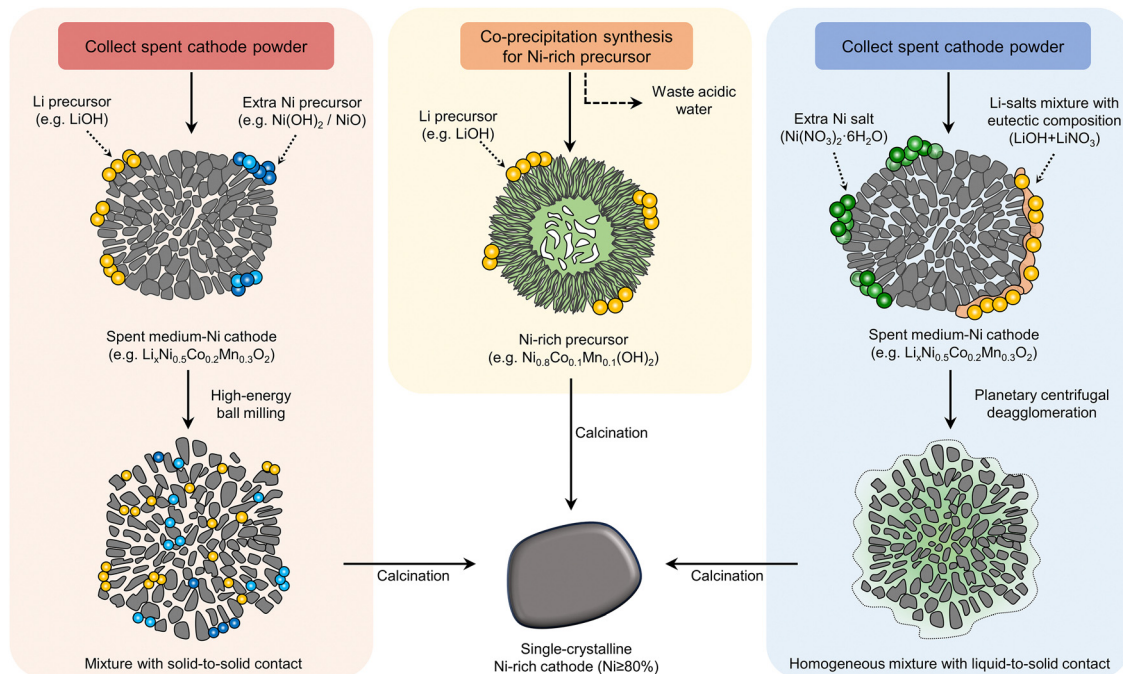


Fig. 1 Schematic comparison of three methods to synthesize Ni-rich single-crystalline cathodes. A conventional solid-state approach involves collecting spent medium-Ni cathode powder (e.g., $\text{Li}_x\text{Ni}_{0.5}\text{Co}_{0.2}\text{Mn}_{0.3}\text{O}_2$) and adding Li and Ni precursors (e.g., LiOH and $\text{Ni}(\text{OH})_2$ or NiO). High-energy ball milling is employed to promote solid-to-solid contact among particles, forming a solid-state mixture that undergoes calcination to yield a Ni-rich cathode (left). The co-precipitation synthesis route fabricates a Ni-rich precursor (e.g., $\text{Ni}_{0.8}\text{Co}_{0.1}\text{Mn}_{0.1}(\text{OH})_2$) mixing with LiOH, followed by calcination. This method provides compositional homogeneity, but it generates acidic wastewater as a by-product (middle). The liquified-salts-assisted upcycling approach utilizes a eutectic mixture of LiNO_3 –LiOH with additional $\text{Ni}(\text{NO}_3)_2 \cdot 6\text{H}_2\text{O}$ as a Ni source. Planetary centrifugal deagglomeration promotes liquid-to-solid contact between the liquified salts and spent cathode powder, resulting in a homogeneously distributed mixture and high-quality single-crystalline Ni-rich cathode (right).

NCM523 with LiOH– LiNO_3 (40 : 60 molar ratio at the eutectic composition) and additional $\text{Ni}(\text{NO}_3)_2 \cdot 6\text{H}_2\text{O}$ (to increase the Ni concentration from Ni 50% to Ni 80%) in the planetary centrifugal mixer at 2000 rpm without adding any grinding media. The amount of LiOH– LiNO_3 mixture was carefully calculated to account for both the Li deficiency in the spent NCM523 and the additional Li required for re-synthesizing the NCM811 layered cathode material (Table S1, ESI[†]).

As shown in Fig. 2(a)–(e), we observed distinct and rapid morphological changes in the mixture upon increasing mixing time. Initially, the raw chemicals exhibited distinct colors (green, white, and black) and morphologies (Fig. 2(a)), but after just 3 minutes of planetary centrifugal mixing, the mixture transformed into a uniform black color with wet powder morphology (Fig. 2(b)). Continued mixing for up to 6 min and 12 min further changed the mixture into a slurry-like form (Fig. 2(c)–(e)). This morphological evolution was well correlated with the microstructure observed *via* scanning electron microscopy (SEM). In comparison to the spent NCM523 cathode with secondary particle morphology, we found the primary particles of the NCM523 were well dispersed in the liquified matrix of eutectic LiOH– LiNO_3 and $\text{Ni}(\text{NO}_3)_2 \cdot 6\text{H}_2\text{O}$ (Fig. 2(f) and (g) and Fig. S3, ESI[†]). The secondary particles became fully separated and embedded in a viscous and liquid-like matrix. Energy dispersive X-ray (EDS) mapping confirmed uniform elemental distributions (O, N and Ni; Fig. 2(h) and Fig. S3, ESI[†]),

indicating that the spent NCM523 and liquified salts, including eutectic LiOH– LiNO_3 and $\text{Ni}(\text{NO}_3)_2 \cdot 6\text{H}_2\text{O}$ were uniformly integrated on a fine scale.

Along with the drastic microstructure changes, we observed intriguing phase evolution in the mixture through X-ray diffraction (XRD) analysis (Fig. 2(i)). The spent NCM523 in a slurry-like mixture remains in the layered structure before and after the planetary centrifugal mixing. However, the XRD peaks corresponding to $\text{Ni}(\text{NO}_3)_2 \cdot 6\text{H}_2\text{O}$ gradually diminished, disappearing after 6 min of mixing (note that the XRD results are measured *ex situ* immediately after planetary centrifugal mixing, as shown in Fig. 2(i)). The behavior of the slurry-like mixture during planetary centrifugal mixing aligns with our previous study,^{32,33} implying that the frictional forces between the mixed particles help reach an ‘effective’ temperature exceeding the melting points of LiOH– LiNO_3 eutectic ($T_m = 183\text{ }^\circ\text{C}$) and $\text{Ni}(\text{NO}_3)_2 \cdot 6\text{H}_2\text{O}$ ($T_m = 56.7\text{ }^\circ\text{C}$) (Fig. S4, ESI[†]). Furthermore, we propose that the rapid transition from solid to a liquid-like phase within the 6 minutes of mixing could be facilitated by the presence of hydrates in the $\text{Ni}(\text{NO}_3)_2 \cdot 6\text{H}_2\text{O}$ precursors. The hydrates are known to reduce the energy required for dissolution, thus promoting an early liquid-like environment and enhancing homogeneity in element distribution during planetary centrifugal mixing. Also, considering a density of 2.05 g cm^{-3} for $\text{Ni}(\text{NO}_3)_2 \cdot 6\text{H}_2\text{O}$ and 4.80 g cm^{-3} for layered-type oxide, we estimated the volume ratio of the liquified nitrates to the oxide is about 11 : 1, which is sufficient to effectively wet and



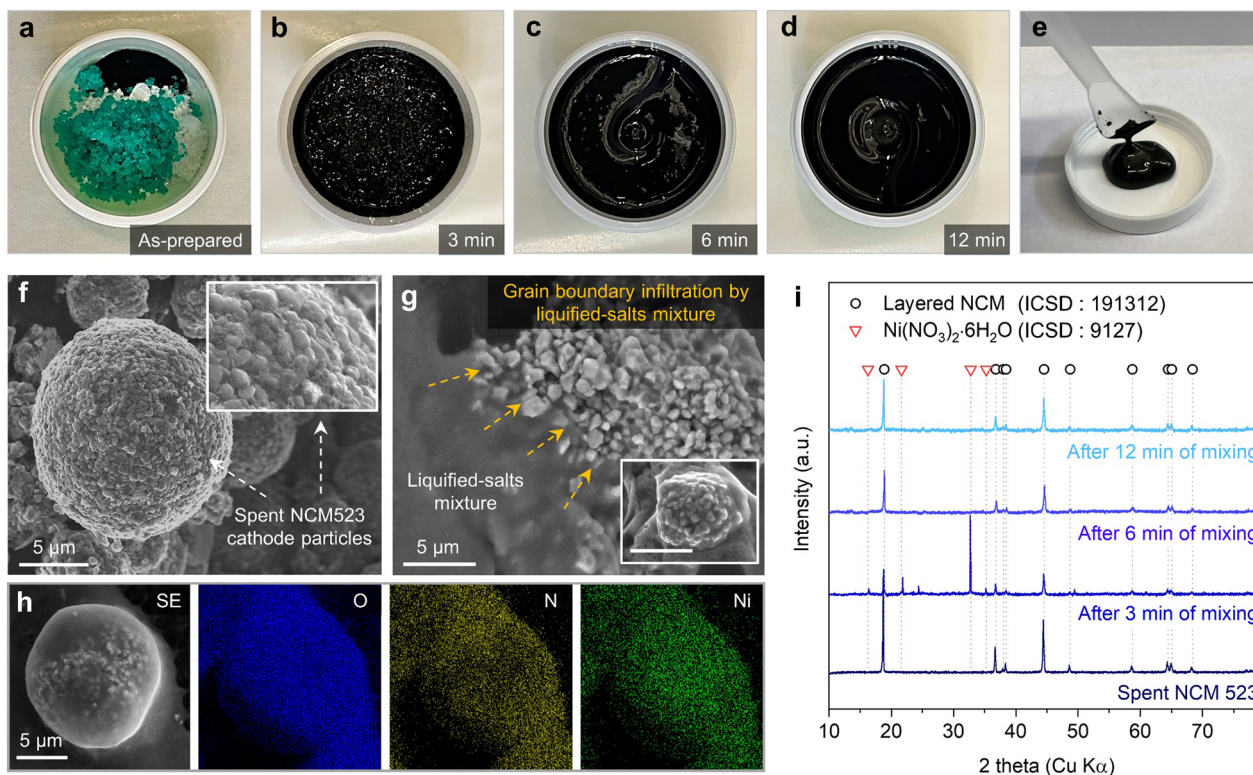


Fig. 2 Morphological and structural evolution of spent NCM523 during the liquified-salts-assisted upcycling process. (a)–(e) Digital images of the spent NCM523 cathode material as it undergoes liquified-salts-assisted upcycling through planetary centrifugal mixing. (a) The initial state of the dry, as-prepared mixture, followed by stages at (b) 3 min, (c) 6 min and (d) and (e) 12 min of mixing spent NCM523 powder with LiOH–LiNO₃ (as Li source) and Ni(NO₃)₂·6H₂O (as Ni source). (f) and (g) SEM images of the powder mixture in the as-prepared state and after 12 min mixing. (h) Secondary-electron (SE) image and EDS mapping of O, N, and Ni of the powder mixture after 12 min of mixing. (i) XRD patterns of the mixture of spent NCM523 powder with LiOH–LiNO₃ and Ni(NO₃)₂·6H₂O at different mixing times.

fully separate the primary particles of the spent NCM523 cathode.³⁴ As a result, the liquefaction of the LiOH–LiNO₃–Ni(NO₃)₂·6H₂O mixture accelerated by multiple hydrates enables the deagglomeration of spent NCM523 particles, and this allows them to become separately embedded within the liquified matrix, thus fostering intimate contacts among precursors and the formation of a dense colloidal suspension.

Chemical and microstructural upcycling

Fig. 3 compares the microstructure, phase composition, and elemental distribution between Ni-rich cathodes (target composition: Li_{1.0}Ni_{0.80}Co_{0.08}Mn_{0.12}O₂) re-synthesized *via* a conventional solid-state direct upcycling method (SS-NCM) and those processed by the new liquified-salts-assisted upcycling method (LS-NCM). We selected SS-NCM as a reference because it is conventionally re-synthesized by using Ni(OH)₂ and LiOH, providing a suitable baseline for evaluating the benefits introduced by liquified-salts-assisted upcycling. In the synthesis process of SS-NCM, we used a lab-scale mechanical mixer with additional hand grinding instead of high-energy ball-milling to identify the significant effect of the mixer type on the performance of the cathode material. Fig. 3(a) and (d) depict the morphology of SS-NCM and LS-NCM cathodes, respectively, as observed by SEM. Despite their relatively small primary particle

size, SS-NCM particles are heavily agglomerated as consistent with typical microstructural features for solid-state synthesis (Fig. S5, ESI[†]). In contrast, LS-NCM has more uniformly distributed micro-sized particles and fewer agglomerates, indicating that the liquified-salts-assisted method facilitates more uniform particle dispersion and a smoother surface morphology. The less agglomerated LS-NCM than SS-NCM is further supported by smaller *D*₅₀ in particle size distribution and smaller surface area of the former (Table S2 and Fig. S6, ESI[†]). The enhancement in particle uniformity can provide consistency in the quality of the electrode fabrication process, and also reduces inconsistency in electrochemical reactions.

In addition, with the morphology difference between SS-NCM and LS-NCM, we also revealed that liquified-salts contribute significantly to structural modification. Through high-angle annular dark-field scanning transmission electron microscopy (HAADF-STEM) and high-resolution transmission electron microscopy (HR-TEM) analysis, we observed an evolution of multiple inter-granular cracks with extensive void defects and rock-salt structure in spent NCM523, which is consistent with a deteriorated NCM523 cathode (Fig. S7, ESI[†]).^{35,36} After the solid-state upcycling process, the HAADF-STEM images of SS-NCM show a rock-salt structure with ~10 nm thickness covering the combined layered and rock-salt structure beneath, and the corresponding



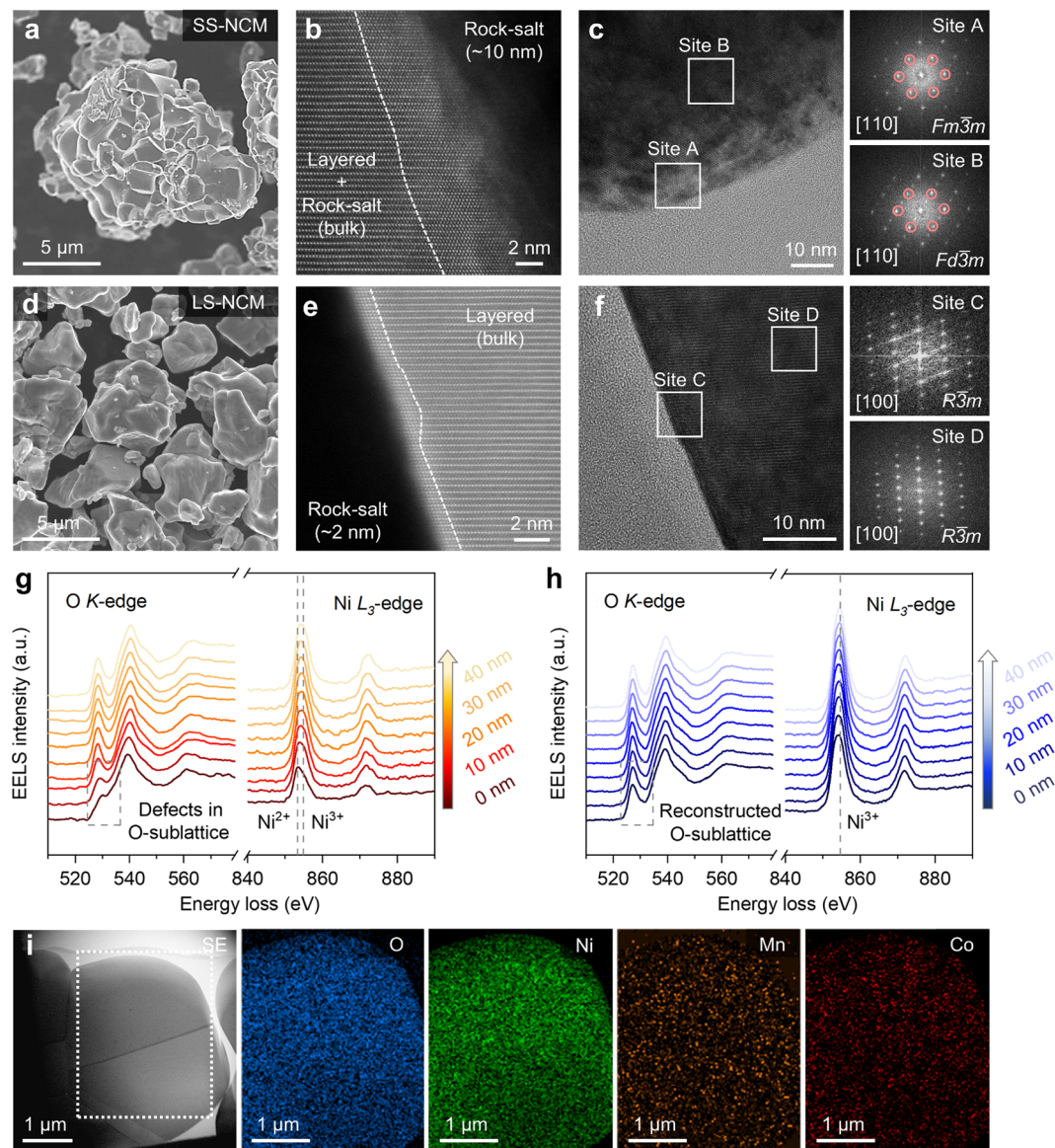


Fig. 3 Chemical and structural characterizations of micro-sized LS-NCM. (a)–(h) Comparative microstructural, crystallographic, and elemental analysis of SS-NCM and LS-NCM cathodes. (a)–(c) SEM images, HAADF-STEM, and HR-TEM with FFT patterns of SS-NCM. (d)–(f) SEM images, HAADF-STEM, and HR-TEM with FFT patterns of LS-NCM. (g) and (h) EELS line scan profile of SS-NCM (red, left) and LS-NCM (blue, right) measured from the outer surface (0 nm) to inner surface of 40 nm depth. (i) TEM image and EDS mapping results of LS-NCM in the corresponding region.

region indicates $Fd\bar{3}m$ symmetry after fast-Fourier transform (FFT) in the HR-TEM results (Fig. 3(b) and (c)). In comparison, LS-NCM exhibited a notably thinner rock-salt layer ($Fm\bar{3}m$ symmetry) of approximately ~ 2 nm along the sub-surface, and the bulk layered phase with $R\bar{3}m$ symmetry (Fig. 3(e) and (f)). From electron energy loss spectroscopy (EELS) measurements, severe Ni reduction (Ni^{3+} reduced to Ni^{2+} shown by the Ni L_3 -edge) and defects in the oxygen sublattice (shown by the O K-edge) are observed in SS-NCM (Fig. 3(g)). In contrast, even at the surface of LS-NCM, Ni reduction and oxygen defects are rarely observed (Fig. 3(h), EELS scanning pathway on SS-NCM and LS-NCM are listed in Fig. S8, ESI[†]). The differences in sub-surface structure between SS-NCM and LS-NCM can be attributed to the manner in which the spent NCM523 powder is packed with Li- and Ni-based precursors. In

the solid-state synthesis of SS-NCM, solid–solid contacts predominate, thus defects (such as gradients in oxygen vacancies and Ni concentration) are likely to accumulate along the surfaces of the spent NCM523 particles, especially near the solid–solid junctions, due to the lack of a fluid medium. Indeed, through TEM-EDS analysis, we found localized Ni-rich regions on the surface and along the grain boundaries of SS-NCM particles (Fig. S9, ESI[†]). However, in LS-NCM synthesis, the early liquified salts can act as a diffusion medium that facilitates uniform distribution of Li and Ni ions and restoration of the lattice composition within the cathode particle matrix, thereby minimizing defects and reconstructing the sub-surface from rock-salt into a layered-structure. The compositional uniformity in LS-NCM can be further confirmed by Fig. 3(i) and Fig. S10 (ESI[†]), and these



surface and lattice structural features influence the electrochemical performance, especially for the cycling stability.

Accelerated phase evolution by liquified salt treatment

By using a high-temperature XRD (HT-XRD) technique, we next investigated the effect of liquified salts on phase evolution and structural restoration in LS-NCM during the high-temperature synthesis, and compared it with SS-NCM. Fig. 4 shows the contour maps of HT-XRD data and phase fractions of SS-NCM and LS-NCM measured at each temperature. For SS-NCM, the diffraction peaks corresponding to the spent NCM523 phase and $\text{Ni}(\text{OH})_2$ are observed below 300 °C (Fig. 4(a)). As the temperature increases, partial decomposition of $\text{Ni}(\text{OH})_2$ occurs and leads to the formation of the rock-salt phase (RS), evidenced by the $(200)_{\text{RS}}$ at $2\theta \approx 43.3^\circ$ (Fig. S11a, ESI[†]). By 500 °C, the rock-salt phase becomes prominent and coexists with the layered structure (L), as indicated by the $(104)_{\text{L}}$ peak at $2\theta \approx 43.9^\circ$. The layered structure gradually dominates the XRD pattern of SS-NCM as the temperature increases to ~ 800 °C. However, residual rock-salt domains persist, as evidenced by the negative peak shifts of $(102)_{\text{L}}$ toward $(111)_{\text{RS}}$ and $(104)_{\text{L}}$ toward $(200)_{\text{RS}}$ (Fig. 4(a) and Fig. S11a, ESI[†]).³⁷ The phase-fraction analysis in Fig. 4(b) also confirms a significant proportion of the rock-salt phase remains alongside the formation of

the layered phase. The persistence of the rock-salt phase at higher temperatures in SS-NCM highlights the limitations of the solid-state method for the upcycling process, particularly its inability to achieve complete structural restoration due to insufficient precursor distribution and limited ionic diffusion.

In contrast, the LS-NCM cathode synthesized using a eutectic mixture of LiOH-LiNO_3 and $\text{Ni}(\text{NO}_3)_2 \cdot 6\text{H}_2\text{O}$ as precursors exhibited a layered structure with significantly fewer impurities compared to SS-NCM (Fig. 4(c)). Below 300 °C, the diffraction peaks indicate the coexistence of spent NCM 523 and the $\text{Ni}(\text{NO}_3)_2$ precursors. As the temperature increases, $\text{Ni}(\text{NO}_3)_2$ decomposes into the rock-salt phase, initiating the formation of transient rock-salt phases between 300 °C and 500 °C. However, unlike in SS-NCM, the rock-salt phase in LS-NCM diminished rapidly beyond ~ 500 °C, and the diffraction peaks corresponding to the layered structure (e.g., $(003)_{\text{L}}$, $(104)_{\text{L}}$) dominate the XRD pattern up to ~ 800 °C (Fig. S11b, ESI[†]). This observation fairly aligns with the TEM results of LS-NCM, which exhibit a thin rock-salt layer along the outer surface of LS-NCM with much less cation-mixing than in SS-NCM (Fig. S12 and Table S3, ESI[†]). The rapid recession of the rock-salt phase in LS-NCM can be attributed to nanoscale dispersion and intimate interfacial interaction facilitated by liquified salts. During SS-NCM synthesis, the limited contact between the solid

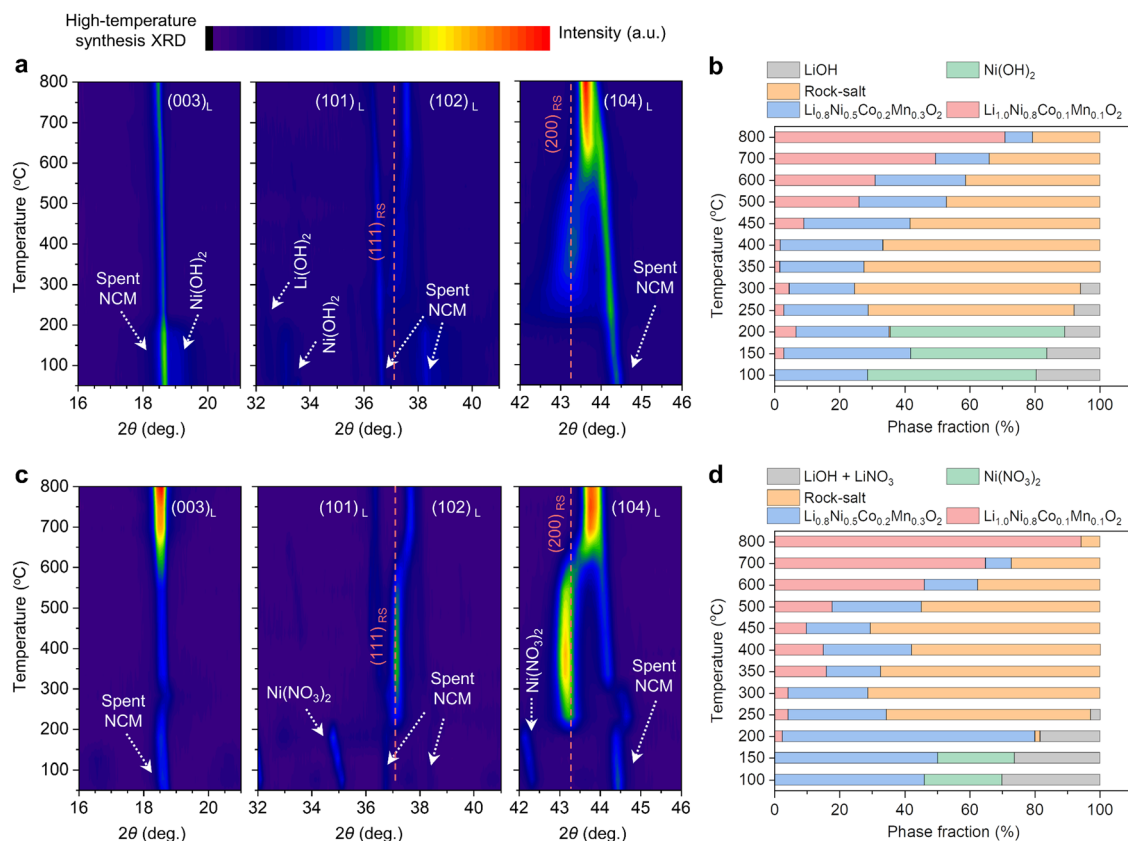


Fig. 4 Comparison of phase evolution in SS-NCM and LS-NCM during high-temperature annealing. (a) and (b) Contour maps of HT-XRD patterns of the mixture of spent NCM523 with LiOH and $\text{Ni}(\text{OH})_2$, and phase fraction during the annealing process for SS-NCM synthesis. (c) and (d) Contour maps of the HT-XRD patterns of the mixture of spent NCM523 with a eutectic mixture of LiOH-LiNO₃ and $\text{Ni}(\text{NO}_3)_2$ and phase fraction during the high-temperature annealing process for LS-NCM synthesis.



precursors and spent NCM523 creates localized Ni-rich regions, where nickel is poorly incorporated into the lattice of spent NCM523. These regions stabilize the rock-salt phase, decelerating its complete conversion to the desired layered structure even at 800 °C. In contrast, in LS-NCM, the homogeneous dispersion of nickel and lithium elements *via* liquified-salts ensures that any rock-salt domains form as nanoscale clusters, almost fully surrounded by the spent NCM523 cathode. The nanoscale rock-salt domains exhibit physical properties analogous to those observed in systems undergoing melting-point depression.^{38,39} The nanoscale rock-salt domains, with high surface-to-volume (S-to-V) ratio, render them thermodynamically unstable, leading to weakened atomic interactions at the surface and thus enabling their rapid dissolution into Li- and oxygen-rich environments.⁴⁰ The liquid phase formed by the eutectic Li-salts facilitates enhanced ion diffusion and promotes the reorganization of nickel, lithium, and oxygen within the cathode lattice.^{41,42} As a result, larger and more stable spent NCM523 particles (with lower S-to-V ratio) grow at their expense, and the Ni in rock-salt phase are successfully incorporated into the layered structure as the temperature increases. Furthermore, TEM results confirm the growth of single-crystalline structures in LS-NCM, likely driven by Ostwald ripening, where smaller rock-salt domains dissolve and contribute to the growth of larger, stable layered particles with compositional uniformity.³² The phase-fraction analysis in Fig. 4(d) corroborates these findings, showing the near-complete suppression of the rock-salt phase and the dominance of the Ni-rich layered structure in LS-NCM. The combination of liquified-salts-assisted synthesis and Ostwald ripening establishes LS-NCM as a superior approach for upcycling spent cathodes. By leveraging homogeneous precursor distribution and particle growth mechanisms, this method achieves structural restoration, compositional uniformity, and the suppression of undesirable phases such as rock-salt.

Electrochemical properties of upcycled cathodes

Next, we investigated the electrochemical performance of SS-NCM and LS-NCM as LIB cathodes. When the first cycle was performed at 0.1C (that is, the formation step; 1C defined as 200 mA g⁻¹) between 2.8 V and 4.3 V (*vs.* Li/Li⁺), SS-NCM has a discharge capacity of 192 mA h g⁻¹ and a first-cycle Coulombic efficiency (C.E.) of 84.9%. In comparison, LS-NCM has a slightly higher discharge capacity of 198 mA h g⁻¹ and a higher first-cycle C.E. of 87.3% (Fig. 5(a), the first-cycle capacity and C.E. of reference NCM811 cathode materials are compared in Fig. S13, ESI†). The capacity improvement in both SS-NCM and LS-NCM compared to that of spent NCM523 can be ascribed to increased Ni concentration, leading to an extension of the Ni-redox reaction. Upon cycling at 0.5C charge/1.0C discharge for 100 cycles, LS-NCM has better capacity retention (94.1% for LS-NCM *vs.* 77.6% for SS-NCM) with more stable charge-discharge curves compared to SS-NCM (Fig. 5(b) and Fig. S13, ESI†). Furthermore, LS-NCM exhibits a better rate capability than SS-NCM (151 mA h g⁻¹ for LS-NCM *vs.* 141 mA h g⁻¹ for SS-NCM at 5C, Fig. 5(c) and Fig. S14, ESI†). To gain a better understanding of the improved cycling stability and rate capability, we conducted galvanostatic intermittent titration

technique (GITT) measurements with a titration current of 0.3C after the fifth and last (100th cycle in the total number of 0.5C/1.0C cycling) cycles. Here, we focused on the voltage loss during each relaxation step, which reflects ohmic and non-ohmic loss at each depth-of-discharge. As shown by the discharge profiles in Fig. 5(d), a more severe polarization developed in cycled SS-NCM than in cycled LS-NCM, and the average voltage loss was approximately 1.50 times greater in the former. The more detailed GITT analysis in Fig. S15 (ESI†) demonstrates a higher impedance growth in SS-NCM than in LS-NCM, mostly in the form of ohmic loss (which indicates degraded electron transport at the microstructure level, consistent with a wide range of rock-salt phase formation along the subsurface of SS-NCM); this is further supported by electrochemical impedance spectroscopy (EIS) measurements (Fig. S16, ESI†). In addition, compared with previous literature on Ni-rich cathodes synthesized from fresh or recycled precursors, LS-NCM shows compelling electrochemical performance even at wider voltage ranges from 2.8 to 4.4 V and from 2.8 to 4.5 V (*vs.* Li/Li⁺) (Fig. 5(e) and Fig. S17, Table S4, ESI†). Lastly, to highlight the exceptional performance offered by the liquified-salts-assisted upcycling method, we tested SS-NCM and LS-NCM in 700 mA h-pouch-type full-cells using a spherical graphite (Gr) anode and conducted long-term cycling in the range of 2.8–4.3 V at 25 °C (details of cell design in Table S5, ESI†). As shown in Fig. 5(f) and (g), LS-NCM has an impressive capacity retention of 88.1% (*vs.* 81.2% for SS-NCM) and a high C.E. at 1.0C/1.0C charge/discharge for 300 cycles (more detailed electrochemical performance data are provided in Fig. S18 and S19, ESI†). Given the stable cycling behavior of the Gr anode, the superior cycle life and reduced voltage decay in the LS-NCM/Gr full cell can be attributed to three factors: (i) a thinner and more uniform rock-salt layer that minimizes interfacial resistance and preserves cathode-electrolyte kinetics; (ii) suppressed electrolyte decomposition, leading to improved electrolyte integrity; and (iii) enhanced structural stability of LS-NCM that mitigates transition metal dissolution and subsequent anode-side degradation. These combined effects contribute to the overall reduction in impedance buildup and promote long-term cell durability. Therefore, facile elemental infusion through the intimate solid (spent NCM523) – liquid (Li-/Ni-salts) interface facilitates uniform microstructure modification, thereby resulting in improved electrochemical performance.

Economic and environmental analysis of liquified-salts-assisted upcycling

Using GREET 2020 and EverBatt 2020 software packages developed by Argonne National Laboratory,^{43,44} we conducted a closed-loop life cycle analysis of LIBs, comparing the efficiencies of three upcycling methods depicted in Fig. 6 – pyrometallurgy, hydrometallurgy, and liquified-salts-assisted methods. The prospective cradle-to-gate life cycle assessments (LCA) are applied, consisting of the processes from the collection of individual intermediates from approximately 1.00 kg of spent LIBs (cradle) by different types of reactions to the production of cathode materials using these intermediates as the reaction



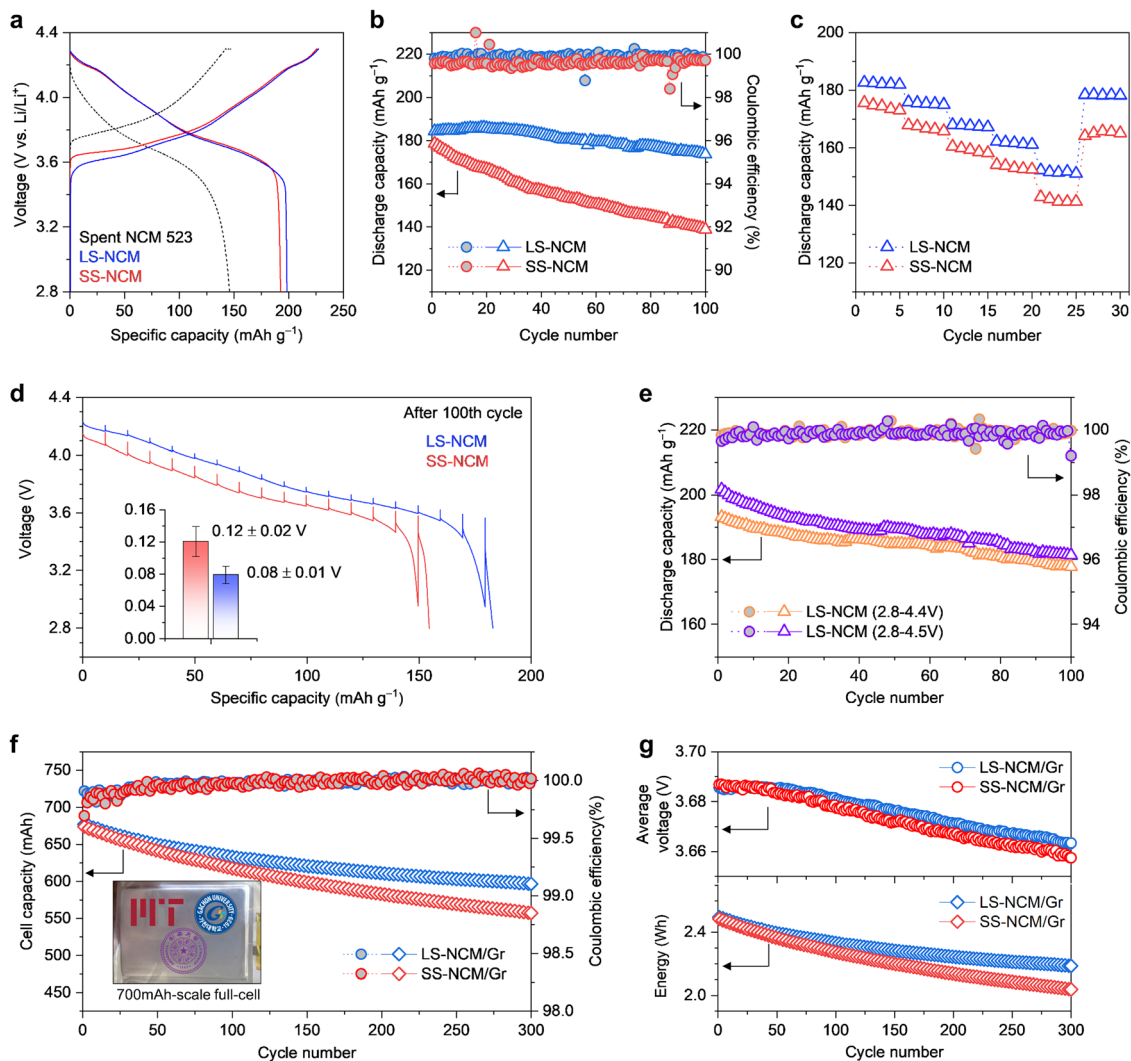


Fig. 5 Superior electrochemical performance of LS-NCM over SS-NCM. (a) Voltage-capacity curves of spent NCM523, LS-NCM and SS-NCM measured at the initial first cycle (formation step) with 0.1C in the voltage ranges of 2.8–4.3 V. (b) and (c) 0.5C charge–1.0C discharge cycling performance and rate charge–1.0C discharge tests of LS-NCM and SS-NCM after the formation step (1C defined as 200 mA g⁻¹). (d) Discharge curves of the GITT measurements conducted after the 100th cycle in (a). Inset: Average voltage loss and its standard deviation (raw data available in Fig. S15, ESI[†]) over different GITT steps. (e) Cycling performance of LS-NCM for 100 cycles at 0.5C charge–1.0C discharge in the voltage ranges of 2.8–4.4 V and 2.8–4.5 V (vs. Li/Li⁺) at 25 °C (1C defined as 210 and 220 mA g⁻¹ for 4.4 and 4.5 cut-off voltage, respectively). (f) and (g) Cycling performance of LS-NCM/Gr and SS-NCM/Gr full-cells at 1.0C in the range of 2.8–4.3 V at 25 °C. Inset: Photo of an assembled pouch cell.

precursors at the factory (gate). The use of spent NCM523 cathode material is considered a major source for the upcycling process, but its disposal (grave) is not considered. A more detailed discussion about LCA is shown in Note S1 (ESI[†]). Each of these upcycling pathways demonstrates distinct process flows, resource requirements, and environmental impacts (Fig. 6). As shown in Fig. 6(a)–(c), the liquified-salts-assisted method is the most environmentally sustainable option in this comparison, achieving high efficiency with minimal resource consumption. The use of low-temperature calcination and innovative mixing methods substantially reduces water and energy requirements and lowers greenhouse gas (GHG) emissions (Tables S6–S10 and Fig. S20, ESI[†]). The liquified-salts-assisted upcycling approach exhibits notably lower energy consumption (4.94 MJ per kg cell) and GHG emissions

(0.68 kg per kg cell) compared to traditional pyrometallurgical and hydrometallurgical recycling methods (Fig. 6(d) and Fig. S20, ESI[†]). Moreover, our method bypasses complex, water-intensive preprocessing steps by directly yielding usable cathode materials. Consequently, the simplified process can potentially lead to enhanced profitability through lower operational expenses, especially compared to destructive methods primarily aimed at recovering metallic precursors from spent cathodes (Fig. S21, ESI[†]). Indeed, among various direct recycling or upcycling strategies evaluated, our liquified-salts-assisted approach consistently demonstrates the lowest environmental impact (in terms of GHG emissions) and energy usage per kilogram of processed battery cells, alongside superior economic viability (Fig. S22, ESI[†]). It should be noted that the cost analysis presented here does not fully reflect the



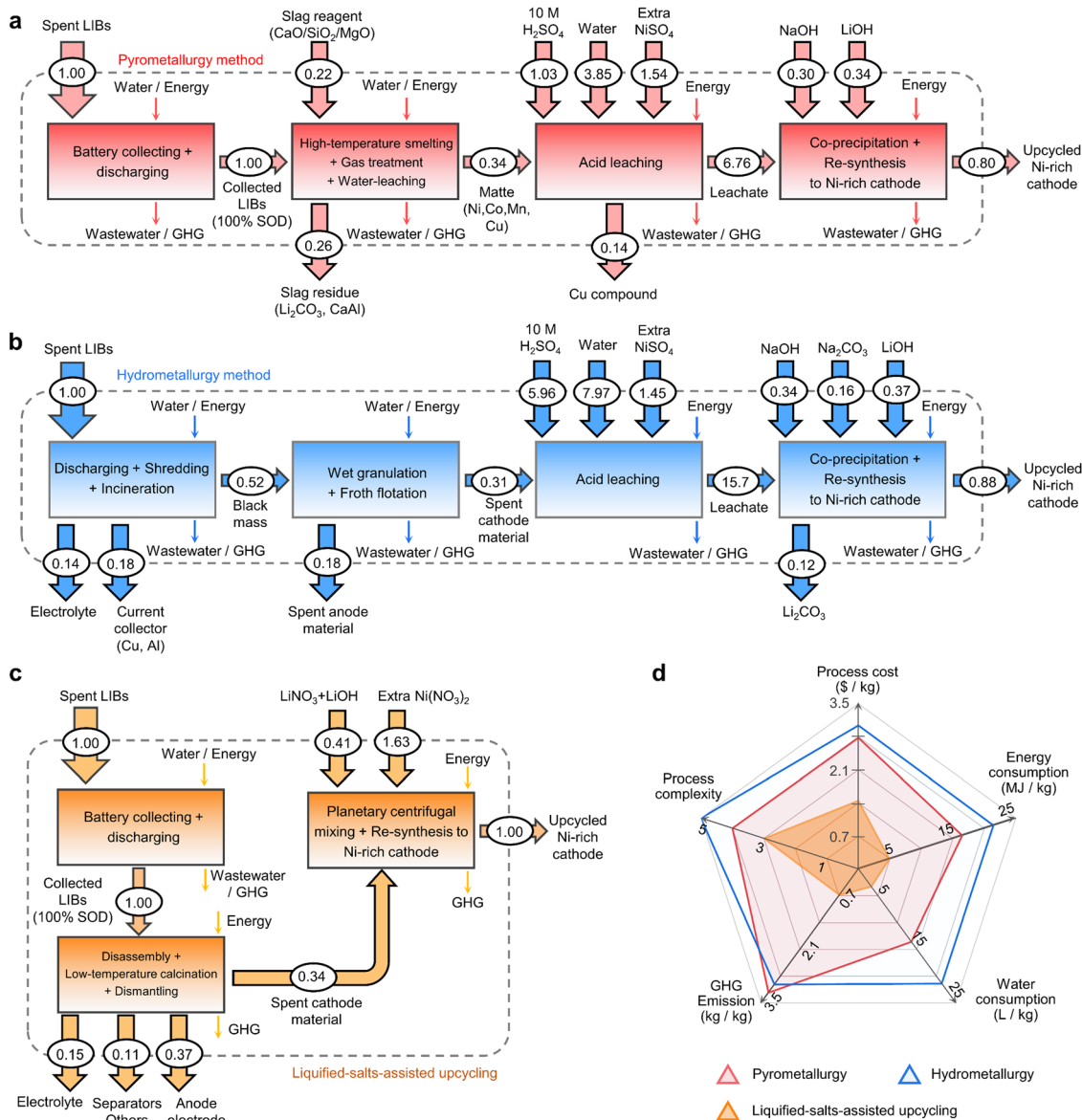


Fig. 6 Economic and environmental analysis of liquified-salts-assisted upcycling method. (a)–(c) Process flow diagrams of various spent lithium-ion battery recycling routes, displaying the life cycle inventory including all considered inputs and outputs. Incidental inputs and outputs are shown with small arrows to differentiate them from explicit inputs and outputs. (a) Pyrometallurgy method, (b) hydrometallurgy method, and (c) liquified-salts-assisted upcycling method. The unit is kg for all material flow. (d) Spider diagram manifesting key features of upcycling methods regarding industrial viability (GHG: greenhouse gas).

complexities associated with industrial-scale deployment, particularly regarding precise quantification of additional Li and Ni, and atmospheric control, due to current methodological limitations. Nevertheless, the compelling combination of minimal energy consumption, lowest GHG emissions, and competitive upcycling costs positions our method as a promising candidate for real-world industrial application. Our approach aligns with the growing demand for cost-effective, low-environmental-impact LIBs upcycling solutions. With increased interest in cathode materials possessing high-Ni concentration and low Co contents, such as $\text{LiNi}_{0.90}\text{Co}_{0.05}\text{Mn}_{0.05}\text{O}_2$ and $\text{LiNi}_{0.80}\text{Co}_{0.15}\text{Al}_{0.05}\text{O}_2$, more economically-efficient recycling with

eco-friendly benefits might be attainable using the liquified-salts-assisted method.

Author contributions

M. Y., Y. D., and J. L. conceived the project. M. Y. and Y. D. designed the experiments and analyzed the data. M. Y. and J. P. synthesized the materials and conducted electrochemical testing. W. C. conducted SEM and *ex situ* XRD measurements. D. S. conducted *in situ* XRD measurements. Y. H. and T. D. analyzed the TEM data. Y. L., J. S. and S. L. designed and assembled



pouch-type full-cells and conducted electrochemical tests. M. Y. calculated the economic and environmental impacts of the upcycling process using EverBatt 2020 and GREET 2020. J. C. contributed to the evaluation and analysis of the study. M. Y., Y. D. and J. L. wrote the paper. All authors discussed and contributed to the writing.

Data availability

Data generated and analyzed in the present work are available in the manuscript and the ESI.†

Conflicts of interest

This work used the methodology reported for the US Provisional Patent Application (US 63/484,989), filed by the MIT Technology Licensing office for our previous work.³² The authors declare no other competing interests.

Acknowledgements

M. Y. acknowledges the support from the National Research Foundation of Korea (NRF) grant funded by the Korea government (Ministry of Science and ICT, MSIT) (RS-2024-00343847). Y. D. acknowledges the support sponsored by Tsinghua-Toyota Joint Research Fund. J. L. acknowledges support from the Defense Advanced Research Projects Agency (DARPA) MINT program under contract number HR001122C0097.

References

- W. Li, E. M. Erickson and A. Manthiram, *Nat. Energy*, 2020, **5**, 26–34.
- R. E. Ciez and J. F. Whitacre, *Nat. Sustainability*, 2019, **2**, 148–156.
- M. Armand and J. M. Tarascon, *Nature*, 2008, **451**, 652–657.
- H.-H. Ryu, H. H. Sun, S.-T. Myung, C. S. Yoon and Y.-K. Sun, *Energy Environ. Sci.*, 2021, **14**, 844–852.
- International Energy Agency (IEA), *Global EV Outlook 2023*, 2023.
- X. Ma, M. Chen, Z. Zheng, D. Bullen, J. Wang, C. Harrison, E. Gratz, Y. Lin, Z. Yang, Y. Zhang, F. Wang, D. Robertson, S.-B. Son, I. Bloom, J. Wen, M. Ge, X. Xiao, W.-K. Lee, M. Tang, Q. Wang, J. Fu, Y. Zhang, B. C. Sousa, R. Arsenaault, P. Karlson, N. Simon and Y. Wang, *Joule*, 2021, **5**, 2955–2970.
- Y. Huang and J. Li, *Adv. Energy Mater.*, 2022, **12**, 2202197.
- M. Fan, X. Chang, Y.-J. Guo, W.-P. Chen, Y.-X. Yin, X. Yang, Q. Meng, L.-J. Wan and Y.-G. Guo, *Energy Environ. Sci.*, 2021, **14**, 1461–1468.
- X. Xiao, L. Wang, Y. Wu, Y. Song, Z. Chen and X. He, *Energy Environ. Sci.*, 2023, **16**, 2856–2868.
- J. Baars, T. Domenech, R. Bleischwitz, H. E. Melin and O. Heidrich, *Nat. Sustainability*, 2021, **4**, 71–79.
- Y. Tao, C. D. Rahn, L. A. Archer and F. You, *Sci. Adv.*, 2021, **7**, eabi7633.
- W. Chen, J. Chen, K. V. Bets, R. V. Salvatierra, K. M. Wyss, G. Gao, C. H. Choi, B. Deng, X. Wang, J. T. Li, C. Kittrell, N. La, L. Eddy, P. Scotland, Y. Cheng, S. Xu, B. Li, M. B. Tomson, Y. Han, B. I. Yakobson and J. M. Tour, *Sci. Adv.*, 2023, **9**, eadh5131.
- G. Harper, R. Sommerville, E. Kendrick, L. Driscoll, P. Slater, R. Stolkin, A. Walton, P. Christensen, O. Heidrich, S. Lambert, A. Abbott, K. Ryder, L. Gaines and P. Anderson, *Nature*, 2019, **575**, 75–86.
- T. Wang, H. Luo, J. Fan, B. P. Thapaliya, Y. Bai, I. Belharouak and S. Dai, *iScience*, 2022, **25**, 103801.
- X. Ma, J. Hou, P. Vanaphuti, Z. Yao, J. Fu, L. Azhari, Y. Liu and Y. Wang, *Chem*, 2022, **8**, 1944–1955.
- G. Qian, Z. Li, Y. Wang, X. Xie, Y. He, J. Li, Y. Zhu, S. Xie, Z. Cheng, H. Che, Y. Shen, L. Chen, X. Huang, P. Pianetta, Z.-F. Ma, Y. Liu and L. Li, *Cell Rep. Phys. Sci.*, 2022, **3**(2), 100741.
- X. Zhang, Y. Bian, S. Xu, E. Fan, Q. Xue, Y. Guan, F. Wu, L. Li and R. Chen, *ACS Sustainable Chem. Eng.*, 2018, **6**, 5959–5968.
- Y. Zheng, S. Wang, Y. Gao, T. Yang, Q. Zhou, W. Song, C. Zeng, H. Wu, C. Feng and J. Liu, *ACS Appl. Energy Mater.*, 2019, **2**, 6952–6959.
- Y. Yao, M. Zhu, Z. Zhao, B. Tong, Y. Fan and Z. Hua, *ACS Sustainable Chem. Eng.*, 2018, **6**, 13611–13627.
- X. Hu, E. Mousa, Y. Tian and G. Ye, *J. Power Sources*, 2021, **483**, 228936.
- J. B. Dunn, L. Gaines, J. C. Kelly, C. James and K. G. Gallagher, *Energy Environ. Sci.*, 2015, **8**, 158–168.
- W. Chu, Y. Zhang, X. Chen, Y. Huang, H. Cui, M. Wang and J. Wang, *J. Power Sources*, 2020, **449**, 227567.
- S. Ko, J. Choi, J. Hong, C. Kim, U. Hwang, M. Kwon, G. Lim, S. S. Sohn, J. Jang, U. Lee, C. B. Park and M. Lee, *Energy Environ. Sci.*, 2024, **17**, 4064–4077.
- Z. Xiao, Y. Yang, Y. Li, X. He, J. Shen, L. Ye, F. Yu, B. Zhang and X. Ou, *Small*, 2024, 2309685.
- J. Wang, J. Ma, Z. Zhuang, Z. Liang, K. Jia, G. Ji, G. Zhou and H.-M. Cheng, *Chem. Rev.*, 2024, **124**, 2839–2887.
- Y. Lan, X. Li, G. Zhou, W. Yao, H.-M. Cheng and Y. Tang, *Adv. Sci.*, 2024, **11**, 2304425.
- A. Banik, T. Famprakis, M. Ghidui, S. Ohno, M. A. Kraft and W. G. Zeier, *Chem. Sci.*, 2021, **12**, 6238–6263.
- X. Meng, J. Hao, H. Cao, X. Lin, P. Ning, X. Zheng, J. Chang, X. Zhang, B. Wang and Z. Sun, *Waste Manage.*, 2019, **84**, 54–63.
- Y. Han, Y. You, C. Hou, X. Xiao, Y. Xing and Y. Zhao, *J. Electrochem. Soc.*, 2021, **168**, 040525.
- J. Jeswiet and A. Szekeres, *Procedia CIRP*, 2016, **48**, 140–145.
- G. Ji, D. Tang, J. Wang, Z. Liang, H. Ji, J. Ma, Z. Zhuang, S. Liu, G. Zhou and H.-M. Cheng, *Nat. Commun.*, 2024, **15**, 4086.
- M. Yoon, Y. Dong, Y. Huang, B. Wang, J. Kim, J.-S. Park, J. Hwang, J. Park, S. J. Kang, J. Cho and J. Li, *Nat. Energy*, 2023, **8**, 482–491.
- H. Yang, C.-A. Wang and Y. Dong, *Adv. Powder Mater.*, 2024, **3**, 100185.



- 34 L. Berger and S. A. Friedberg, *J. Appl. Phys.*, 1965, **36**, 1158.
- 35 S. Klein, P. Bärmann, T. Beuse, K. Borzutzki, J. E. Frerichs, J. Kasnatscheew, M. Winter and T. Placke, *ChemSusChem*, 2021, **14**, 595–613.
- 36 W. Sha, Y. Guo, D. Cheng, Q. Han, P. Lou, M. Guan, S. Tang, X. Zhang, S. Lu, S. Cheng and Y.-C. Cao, *npj Comput. Mater.*, 2022, **8**, 223.
- 37 J. Zhao, W. Zhang, A. Huq, S. T. Mixture, B. Zhang, S. Guo, L. Wu, Y. Zhu, Z. Chen, K. Amine, F. Pan, J. Bai and F. Wang, *Adv. Energy Mater.*, 2017, **7**, 1601266.
- 38 P. Buffat and J. P. Borel, *Phys. Rev. A: At., Mol., Opt. Phys.*, 1976, **13**, 2287–2298.
- 39 A. Cao, R. Lu and G. Veser, *Phys. Chem. Chem. Phys.*, 2010, **12**, 13499–13510.
- 40 A. I. Persson, M. W. Larsson, S. Stenström, B. J. Ohlsson, L. Samuelson and L. R. Wallenberg, *Nat. Mater.*, 2004, **3**, 677–681.
- 41 M. Gu, I. Belharouak, A. Genc, Z. Wang, D. Wang, K. Amine, F. Gao, G. Zhou, S. Thevuthasan, D. R. Baer, J.-G. Zhang, N. D. Browning, J. Liu and C. Wang, *Nano Lett.*, 2012, **12**, 5186–5191.
- 42 P. Xiao, W. Li, S. Chen, G. Li, Z. Dai, M. Feng, X. Chen and W. Yang, *ACS Appl. Mater. Interfaces*, 2022, **14**, 31851–31861.
- 43 M. Wang, A. Elgowainy, U. Lee, A. Bafana, P. T. Benavides, A. Burnham, H. Cai, Q. Dai, U. R. Gracida-Alvarez, T. R. Hawkins, P. V. Jaquez, J. C. Kelly, H. Kwon, Z. Lu, X. Liu, L. Ou, P. Sun, O. Winjobi, H. Xu, E. Yoo, G. G. Zaines and G. Zang, *Summary of Expansions and Updates in GREET[®] 2020*, U.S. Department of Energy, Office of Scientific and Technical Information, Lemont, IL, USA, 2020.
- 44 Q. Dai, J. Spangenberg, S. Ahmed, L. Gaines, J. C. Kelly and M. Wang, *EverBatt: A Closed-loop Battery Recycling Cost and Environmental Impacts Model*, 2019.



Electronic Supplementary Information (ESI)

Upcycling spent medium-Ni cathodes via novel liquified salts sourcing

Moonsu Yoon^{1,2}, Jin-Sung Park^{1,3,4}, Weiyin Chen¹, Yimeng Huang¹, Tao Dai¹, Yumin Lee², Jungmin Shin²,
Seungmi Lee², Yongil Kim², Dongsoo Lee², Daiha Shin⁵, Jaephil Cho⁶, Yanhao Dong^{7,*} and Ju Li^{1,8,*}

¹*Department of Nuclear Science and Engineering, Massachusetts Institute of Technology, Cambridge,
Massachusetts 02139, United States*

²*Department of Chemical, Biological and Battery Engineering, Gachon University, Seongnam 13120,
Republic of Korea*

³*Department of Materials Science and Engineering, Ajou University, Suwon 16499, Republic of Korea*

⁴*Department of Energy Systems Research, Ajou University, Suwon 16499, Republic of Korea*

⁵*Metropolitan Seoul Center, Korea Basic Science Institute, Seoul 03759, Republic of Korea*

⁶*Department of Energy Engineering, School of Energy and Chemical Engineering, Ulsan National Institute
of Science and Technology, Ulsan 44919, Republic of Korea*

⁷*State Key Laboratory of New Ceramics and Fine Processing, School of Materials Science and
Engineering, Tsinghua University, Beijing 100084, China*

⁸*Department of Material Science and Engineering, Massachusetts Institute of Technology, Cambridge,
Massachusetts 02139, United States*

*Corresponding authors. Email: dongyanhao@tsinghua.edu.cn (Y.D.), liju@mit.edu (J.L.).

Table of contents

Experimental Details	Page 2-3
Note S1	Page 4-5
Fig. S1-S22	Page 6-27
Tables S1-S10	Page 28-39
Supplementary References	Page 40-41

Experimental Details

Material synthesis

Double-sided coated cathode sheets, composed of NCM523, carbon black and poly(vinylidene fluoride) (PVDF, as the binder), were obtained from spent batteries (cylindrical cells with a nominal capacity of 3000 mAh) with a capacity retention of approximately 80%. Subsequently, the cathode sheets were thermally treated at 400°C for 20 min to reduce the adhesivity of PVDF binder, facilitating the separation of the cathode powder from the aluminum foil. The separated cathode powder was collected and stored in the argon-filled glove box with an extremely low level of O₂/H₂O (below 0.1ppm).

To transform the deteriorated NCM523 (Li_{1-x}Ni_{0.5}Co_{0.2}Mn_{0.3}O₂) into LS-NCM, 10g of spent cathode powder was mixed with 0.078mol of LiOH·H₂O (99.9%, Sigma Aldrich), 0.116mol of LiNO₃ (99.9%, Sigma Aldrich) at the eutectic composition, and 0.163 mol of NiNO₃·6H₂O (98.5%, Sigma Aldrich) using a planetary centrifugal mixer (ARE-310, THINKY) at 2,000 rpm (around 510 g force) for 12 min. The molar ratio of transition metal to Li was set to 1:1.03. The planetary-centrifugally mixed powders were calcinated at 920°C for 2 h and then at 760°C for 8 h in flowing oxygen. For SS-NCM synthesis, the spent NCM523 cathode powder was mixed with LiOH·H₂O and NiOH (60.0-70.0%, Sigma Aldrich) by using planetary-centrifugal mixer in a 1:1.03 molar ratio of transition metal to Li for 30 min. The mixture was then subjected to calcine at 920 °C for 2 h and then at 760 °C for 8 h in an oxygen atmosphere. The venting line was securely connected outside at the opposite side of the tube furnace to exhaust the gas naturally. Using this venting line, the gas pressure of the furnace can be maintained, and gas products (e.g., toxic NO_x) are effectively removed.

Electrochemical measurements

For electrochemical measurements, the electrodes were fabricated by mixing 90 wt% of cathode active material, 5 wt% of super-P (as the conductive agent), and 5 wt% of poly(vinylidene fluoride) (PVDF, as the binder) in N-methyl-2-pyrrolidone (NMP). The slurry was coated onto aluminum foil and dried at 120°C for 2 h, followed by vacuum-drying for 10 h prior to cell assembly. All cathodes were controlled with a loading level of 12.0 ± 0.5 mg cm⁻². The prepared electrodes were assembled using 2032R coin type cell in Ar-filled glove box, with cathodes (diameter 12 mm), lithium metal foils (diameter 14 mm, thickness 1 mm) as the counter and reference electrode, respectively, and 1.15 M LiPF₆ in ethylene carbonate/ethyl methyl carbonate/diethyl carbonate with 5wt% fluoroethylene carbonate additive (EC:EMC:DEC = 3/6/1 vol% with 5% FEC; Enchem Co., Ltd) as the electrolyte. The cells were evaluated with constant current-constant voltage mode between 2.8 and 4.3/4.4/4.5 V (vs. Li/Li⁺) at 25°C. The first charge-discharge cycle (as the formation step) was conducted at 0.1 C (for SS-NCM and LS-NCM cathode, 1.0 C is defined as 200, 210, and 220 mA g⁻¹ for cut-off voltage of 4.3, 4.4 and 4.5V, respectively). After the first cycle, the cells were charged and discharged at 0.5 C/1.0 C for 100 cycles. After specific cycles, EIS measurements were conducted on cells charged to 4.3 V (vs. Li/Li⁺) from 1 mHz to 10 MHz and with AC voltage amplitude of 10 mV using Reference 3000 (Gamry Instrument). GITT measurements were carried out following the 5th and 100th

cycles of 0.5 C/1.0 C cycling between 2.8 and 4.3 V (versus Li/Li⁺) with a titration step at 0.3 C of 8 min and a relaxation step of 1 h. To evaluate the rate capability, the cells were charged at 0.5 C and discharged at rates of 0.5, 1.0, 2.0, 3.0, and 5.0 C. For full-cell tests, the upcycled cathode and graphite anode were utilized to assemble 700 mAh-scale pouch-type full-cells. The ratio of negative to positive electrode capacity (N/P ratio) was fixed at 1.07 ± 0.01 . The cathode loading level was 12.04 mg cm^{-2} on each side of the double-side coated Al foil. The anode loading level was 6.88 mg cm^{-2} on the double-side coated Cu foil. The graphite electrode density was 1.52 g cm^{-3} and the cathode density was 3.31 g cm^{-3} . The pouch-type full-cells were assembled in an argon-filled glovebox with a humidity of less than 1%. The separator and liquid electrolytes were the same as those used in coin cells. The weight of the electrolyte used in full-cells was 1.75 g, which corresponded to 2.5 g Ah^{-1} . The cycling voltage window was set at 2.8–4.30 V, and one formation cycle with three pre-cycles was executed at 0.1 C and 0.2 C, respectively, before embarking long-term cycling of 300 cycles at 1 C ($1.0 \text{ C} \approx 2.21 \text{ mA cm}^{-2}$ for full-cell). All electrochemical assessments (except for EIS) were performed using a CT2001A battery cycler (Landt Instrument).

Characterizations

The chemical compositions of prepared cathode powders were determined by an inductively coupled plasma optical emission spectrometer (ICP-OES, AVIO 550, Perkin Elmer). Phases were characterized by XRD using a parallel beam XRD instrument (X'Pert Pro MPD, Malvern Panalytical, Cu K α with a wavelength of 1.542 Å) at the Korea Basic Science Institute (KBSI) at Seoul Western Center. High-temperature XRD measurements were conducted using an Anton Paar HTK 1200N stage integrated with the diffractometer, enabling the analysis of structural changes under elevated temperatures. The crystallographic analysis was conducted by using PDXL analysis software (Rigaku). Phase identification was performed using PDXL software package, including crystallography open database (COD). The prepared materials were characterized by scanning electron microscopy (SEM, Merlin, Zeiss) equipped with energy dispersive X-ray spectroscopy (EDS, XFlash® 6130, Bruker) detector. For TEM analysis, samples were prepared by a dual-beam focused ion beam (FIB, Helios 450HP, FEI). High-resolution TEM (HR-TEM, ARM300, JEOL) was conducted under 150 and 300 keV to collect scanning transmission electron microscopy (STEM) images for atomic and structural analysis. Electron energy loss spectroscopy (EELS) and energy dispersive X-ray spectroscopy (EDX) were conducted by HR-TEM (Aztec, Oxford).

Note S1. Life cycle analysis

1. Goal and scope

The closed-loop life cycle analysis (LCA) evaluates and compares the economic and environmental impacts of recycling waste cathode materials from spent lithium-ion batteries and synthesizing new cathode materials.^{1, 2} The analysis examines critical metrics such as greenhouse gas (GHG) emissions, energy consumption, and water usage across several recycling approaches: hydrometallurgical, pyrometallurgical, and liquified-nitrates-assisted upcycling, as detailed in this study. To provide a baseline for comparison, the production of cathode materials from virgin materials is also analyzed. The scope excludes costs related to material transportation and GHG disposal. However, the analysis accounts for raw material expenses, manufacturing costs, and fixed annual capital investments. Energy costs are based on \$0.04 per kWh (1 Wh \approx 3600 J), while water costs are set at \$0.0189 per liter with wastewater discharge fees of \$0.0265 per liter. General expense (\sim 30% of process cost) and overhead costs (\sim 15% of manufacturing cost including resources) are also considered.

2. Scenario description, system boundaries, and inventory analysis.

Four scenarios were analyzed: (1) pyrometallurgical upcycling, (2) hydrometallurgical upcycling, (3) liquified-nitrates-assisted upcycling, and (4) virgin cathode material (Ni-rich cathode) production. Each scenario assumes the treatment of 1 kg of spent lithium-ion batteries, with material and energy flows standardized in a life cycle inventory (**Tables S7-S9**). The LCA adopts a cradle-to-gate perspective, assessment excludes the usage and disposal stages of the cathode materials, under the assumption that recycled and virgin materials exhibit similar or improved performance during use and recycling.

(Scenario 1 : Pyrometallurgical upcycling method) The process discussed here was modified based on the previous work.³ This method involves direct smelting of spent batteries after a discharge pretreatment. Smelting process operates at approximately 1873 K for 3 hours, decomposing organic impurities and reducing transition metal oxides to metallic forms. During smelting process, gas treatment systems mitigate toxic emissions. Lithium salts combine with aluminum and calcium to form slag as a byproduct (e.g. Li_2CO_3 , CaAl). Lithium can be later recovered either via slag treatment or evaporating lithium during smelting.⁴ Energy consumption for smelting is based on a 36 kW pilot-scale furnace processing 174 kg of material. Subsequent acid leaching (0.86 mol L^{-1} H_2SO_4 solution) dissolves the matte, and virgin metal sulfates are added to tailor the Ni, Mn, and Co ratios to target composition. The adjusted metal sulfate solution is utilized to synthesize Transition metal(TM)-based cathode precursor through co-precipitation process. The co-precipitation process forms transition metal hydroxides at pH 10–11 in a nitrogen atmosphere. TM-based precursors are mixed with lithium hydroxide (Li:TM = 1:1.03) and sintered at 1173 K for 2 hours and 1053 K for 10 hours in a 45 kW furnace handling 245 kg. GHG emissions and energy consumption for each step were modeled using EverBatt 2020 and GREET.

(Scenario 2 : Hydrometallurgical upcycling method) In this scenario, 1 kg of spent lithium-ion batteries undergoes a sequence of pretreatment, separation, and chemical processing to recover cathode

materials. The process begins with the discharge of spent batteries to eliminate residual charge and ensure safety during subsequent handling. Following discharge, the batteries are subjected to crushing and shredding operations to break them into smaller fragments. These steps produce a mixture of materials that includes cathode and anode powders, current collectors, binders, and electrolyte residues. The shredded fragments are calcined at 873 K for 2 hours (6 kW and a mass loading of 227 kg in pilot-scale process) to decompose organic binders, evaporate residual electrolytes, and remove impurities like solid electrolyte interface (SEI) components.³ This step also volatilizes moisture and reduces contamination in downstream processes. After calcination, mechanical separation techniques, including wet granulation, density separation, and froth flotation, isolate cathode powders. Wet granulation facilitates particle disaggregation, while density separation removes heavy components like copper and aluminum. Froth flotation uses surfactants to selectively recover cathode particles. These steps help reduce water consumption and minimize the total amount of acid required for the subsequent leaching step, thus increasing the purity of TM-based precursors. The acid amount used in the leaching process was determined by the solid mass and pulp density (~2%). The concentration of the acid was set as was set as 2.8 mol L⁻¹ (H₂SO₄ solution) to improve leaching efficiency. The remaining processes for treating the leachate and re-synthesizing cathode materials were assumed to be similar to those in the pyrometallurgy method described in Scenario 1.

(Scenario 3 : liquified-nitrates assisted upcycling method) In this scenario, the spent batteries were disassembled to collect the spent cathode electrodes after discharge pretreatment. Some work also used 1-methyl-2-pyrrolidinone to soak the cathode side for ~6 hours to remove the poly(vinylidene fluoride) binder.^{3, 5} Here, a one-step low temperature calcination at 673 K for 20 min was applied to remove the polymer binder, electrolytes, and the formed impurities during electrochemical cycling, which was mainly the organic SEI components on the cathode particles. The energy consumption for low temperature calcination was estimated based on the pilot-scale recycling process using the commercial furnace, whose temperature, power, and mass loading were ~873 K, 6 kW and 227 kg, respectively. After the pretreatment, the spent cathode powder was scrapped and dismantled from Al current collectors. And the spent cathode powder was mixed with LiOH, LiNO₃ and Ni(NO₃)₂ to achieve tailored to the desired ratio of TM (Ni, Co, Mn) with the molar ratio of Li:TM to 1.03. The mixture completely forms homogeneously liquified after 15min of planetary centrifugal mixing. The large-scale planetary centrifugal mixer is set with a power rating of 6 kW and a capacity of 300 kg. Finally, the mixture is sintered at 1173 K for 2 hr and subsequently at 1053K for 8hr to re-lithiate the cathode powder and reconstruct the microstructure. The energy consumption for high temperature calcination was estimated based on the commercial furnace, whose temperature, power, and mass loading were ~1173 K, 40 kW and 245 kg, respectively.³ The cathode powder with high-Ni concentration was regarded as the final product from liquified-nitrate assisted method.

(Scenario 4 : Virgin cathode production) This scenario assesses the production of 0.35 kg of virgin cathode materials derived from mined ores. According to the EverBatt 2020 software, producing virgin cathode materials consumes 37.45 L of water and 127.97 MJ of energy while emitting 8.92 kg of GHG. The estimated production cost is \$20.60 per kg of cathode material.

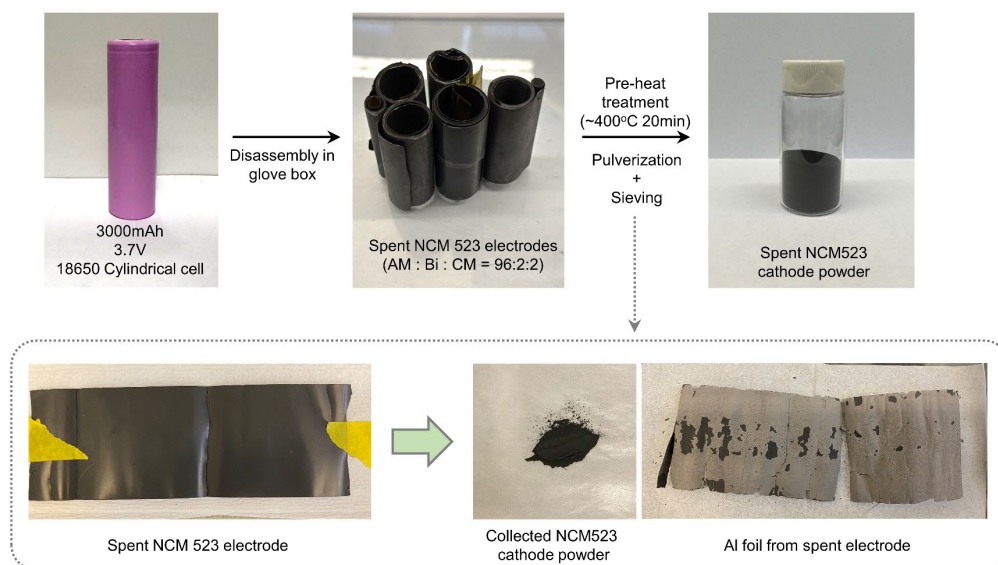


Fig. S1. Process flow for the collection of spent Li_xNi_{0.5}Co_{0.2}Mn_{0.3}O₂ (NCM523, $x \approx 0.7$) cathode powder. The spent commercial cylindrical cell was disassembled, and the spent NCM523 electrodes were retrieved. The electrodes underwent a pre-heat treatment at 400 °C for 20 minutes. Following pre-heat treatment, the NCM523 cathode powder was separated from the aluminum foil using a silicon carbide blade. The separated powder was subsequently pulverized into a fine powder using a mortar, and stored after sieving for further analysis and testing.

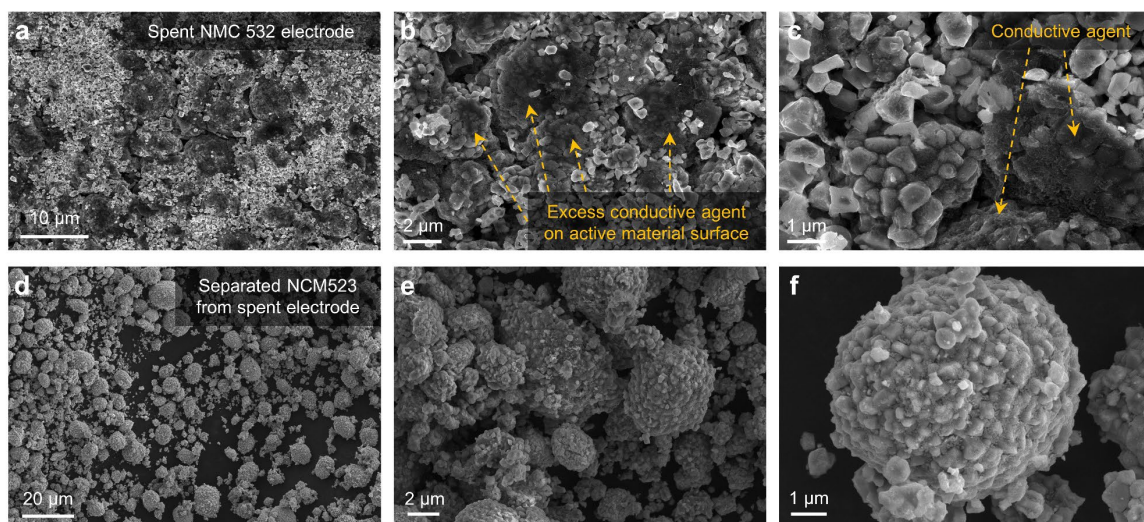


Fig. S2. (a-c) Top-view scanning electron microscopy (SEM) images of spent NCM523 electrode. (d-f) Spent NCM523 cathode powder collected from the electrodes after pre-heat treatment at 400°C for several minutes.

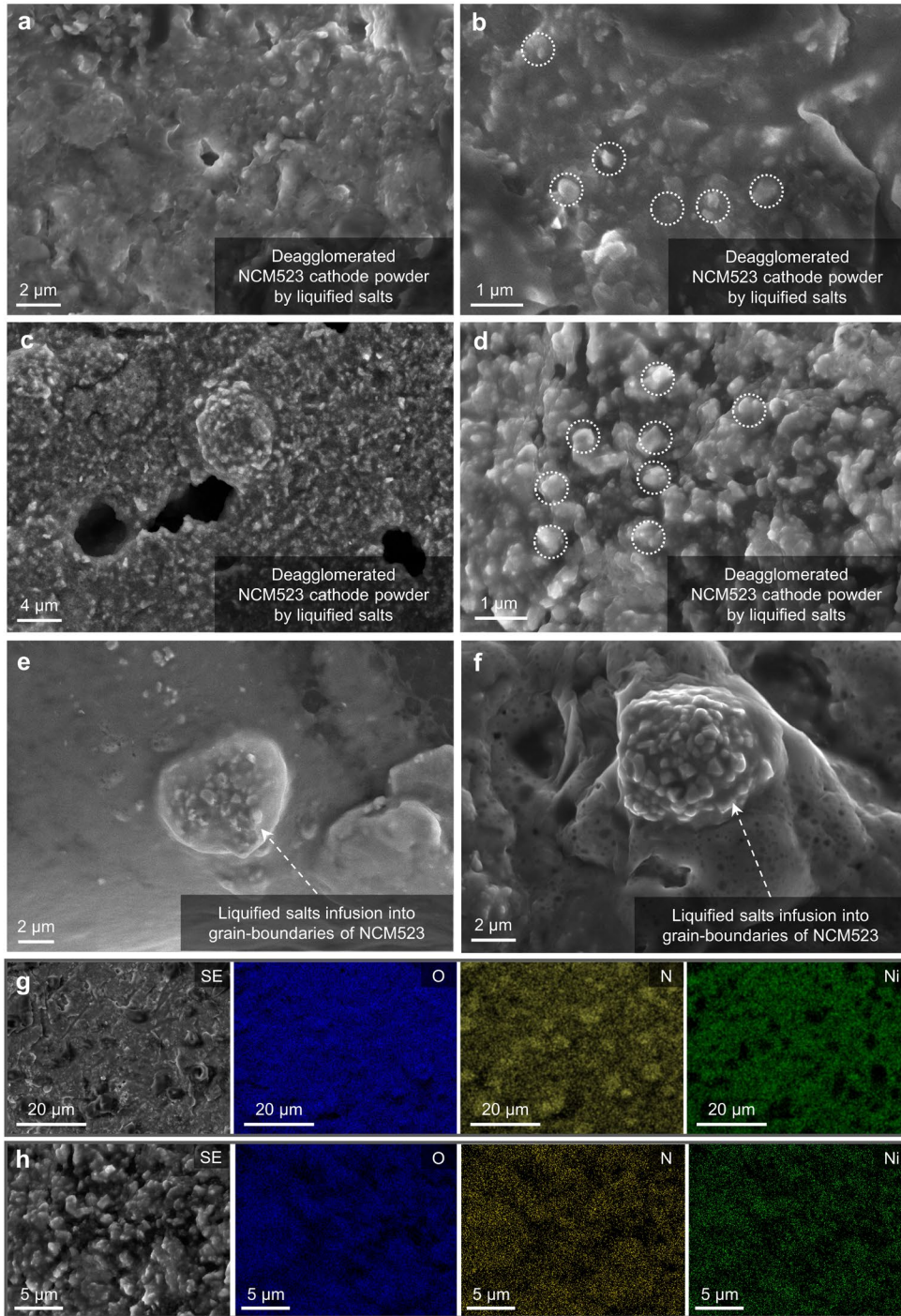


Fig. S3. Deagglomeration of NCM523 secondary particle cathode after planetary centrifugal mixing of 12min. (a-f) SEM images of spent NCM523 particles and Li-/Ni-based liquified molten-salts after planetary centrifugal mixing, and (g, h) corresponding energy dispersive spectroscopy (EDS) mapping results of NCM523 powder with Li-/Ni-based liquified molten-salts

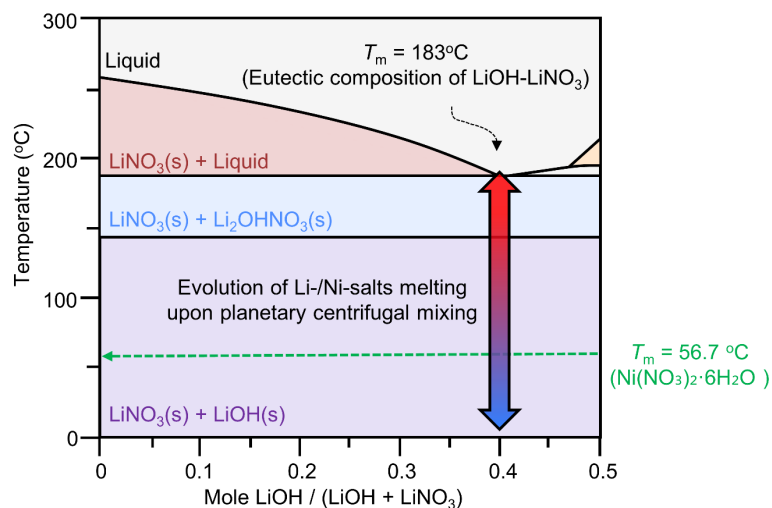


Fig. S4. Phase diagram of LiOH–LiNO₃ system (adapted from FactSage thermochemical software and databases)⁶ with melting temperature of Ni(NO₃)₂·6H₂O. The frictional forces between the mixed particles helps to reach an ‘effective’ temperature higher than the melting points of LiOH–LiNO₃ eutectic ($T_m = 183\text{ °C}$) and Ni(NO₃)₂·6H₂O ($T_m = 56.7\text{ °C}$) during planetary centrifugal mixer.

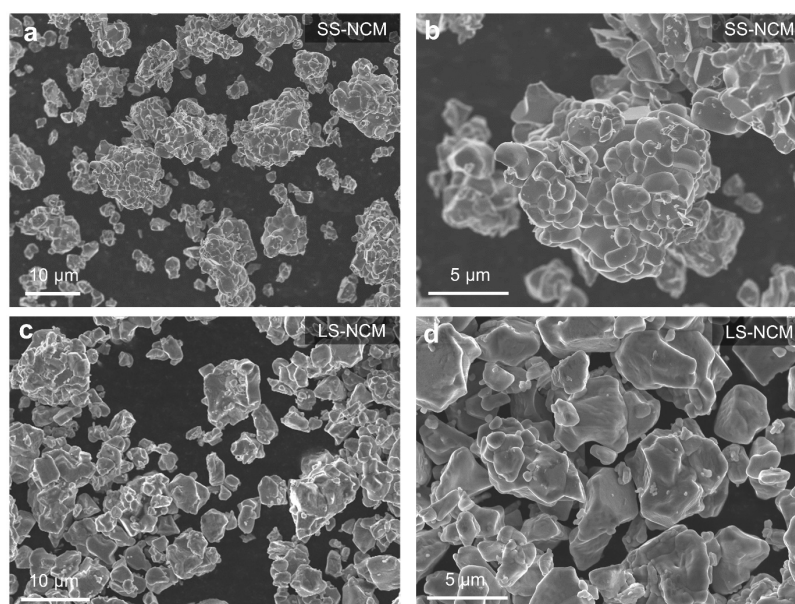


Fig. S5. (a-d) SEM images of SS-NCM and LS-NCM cathode powders. SS-NCM was synthesized from spent NCM523 powder using LiOH and NiOH as precursors. For the synthesis of LS-NCM, a eutectic mixture of LiOH–LiNO₃ and extra Ni(NO₃)₂·6H₂O was used to replenish deficient Li and increase the Ni concentration from ~0.5 to ~0.8.

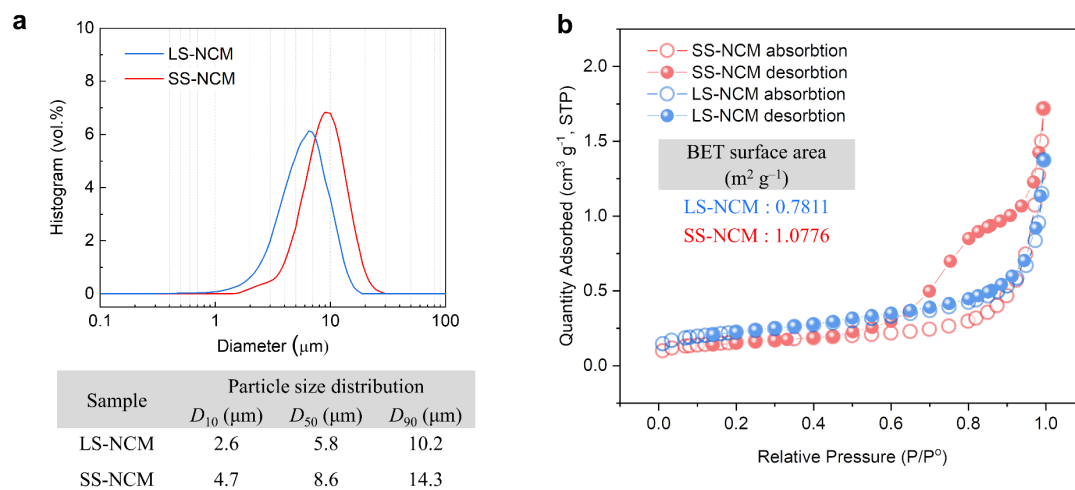


Fig. S6. (a,b) Particle size distribution and surface area of each LS-NCM and SS-NCM

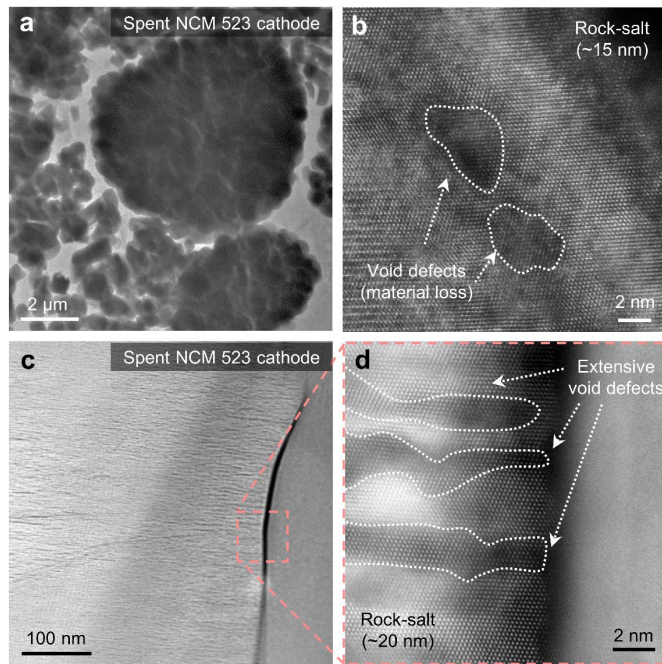


Fig. S7. (a-d) Transmission electron microscope (TEM) and scanning transmission electron microscope (STEM) images of cross-sectioned spent NCM523 cathode particles collected from cylindrical cell.

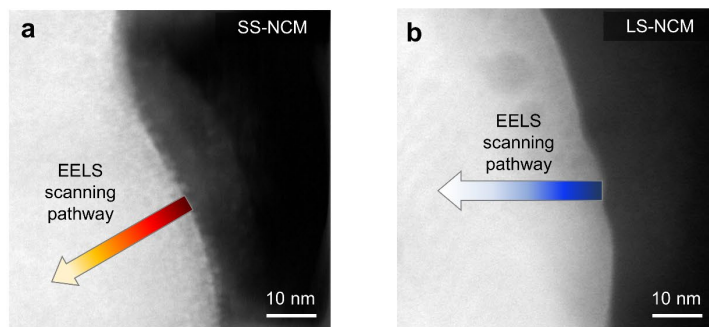


Fig. S8. Schematic STEM-Electron energy loss spectroscopy (EELS) scanning pathway (0 to 40 nm from outer surface) of (a) SS-NCM and (b) LS-NCM, corresponding to EELS profile data in Fig. 3(g) and (h), respectively.

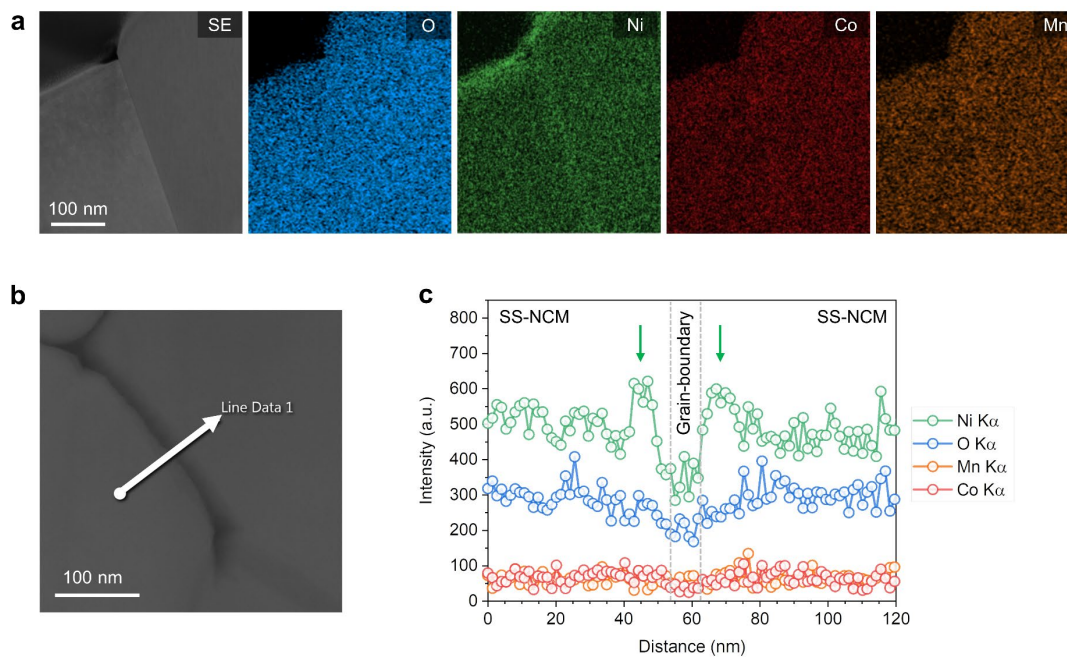


Fig. S9. (a) EDS mapping results of SS-NCM, and (b, c) EDS-line scanning profile and the corresponding region in SS-NCM, showing the inhomogeneity in stoichiometric distribution on the surface of SS-NCM.

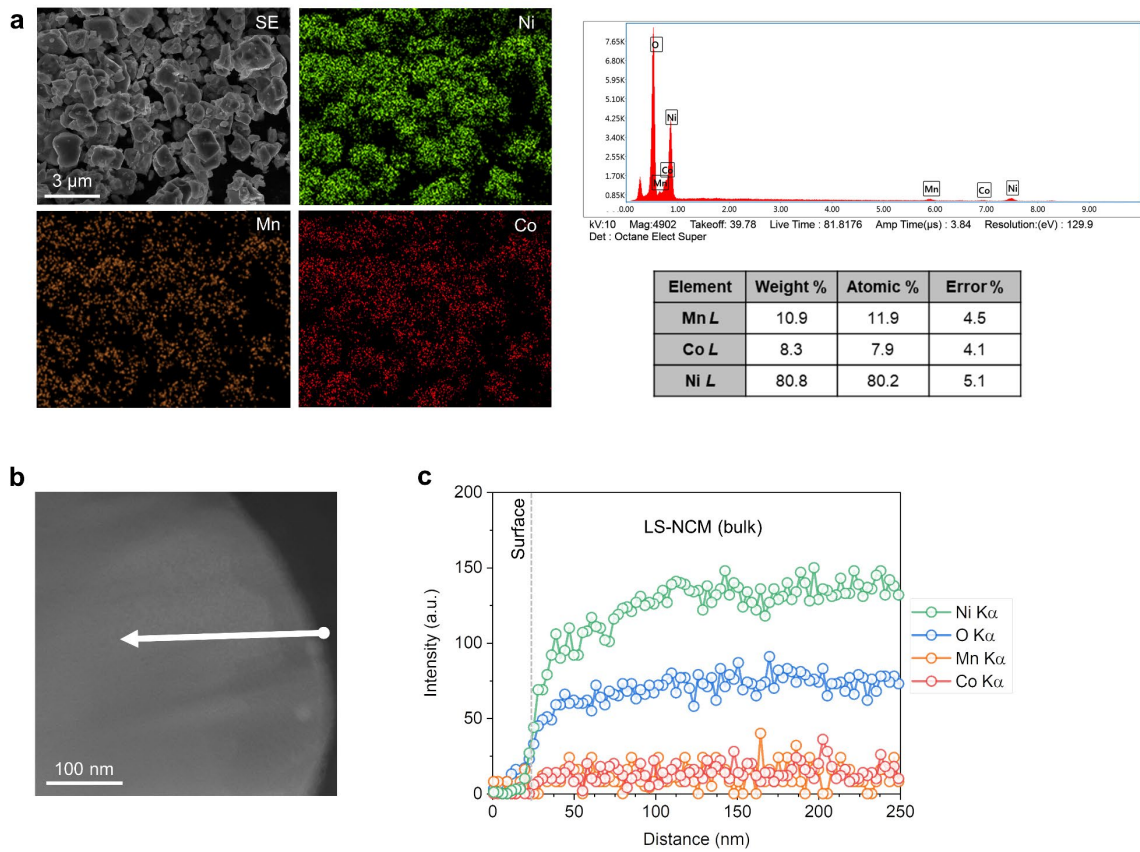


Fig. S10. (a) EDS mapping results and spectra of LS-NCM, and (b, c) EDS-line scanning profile and the corresponding region in LS-NCM, showing the stoichiometric coherence with target composition.

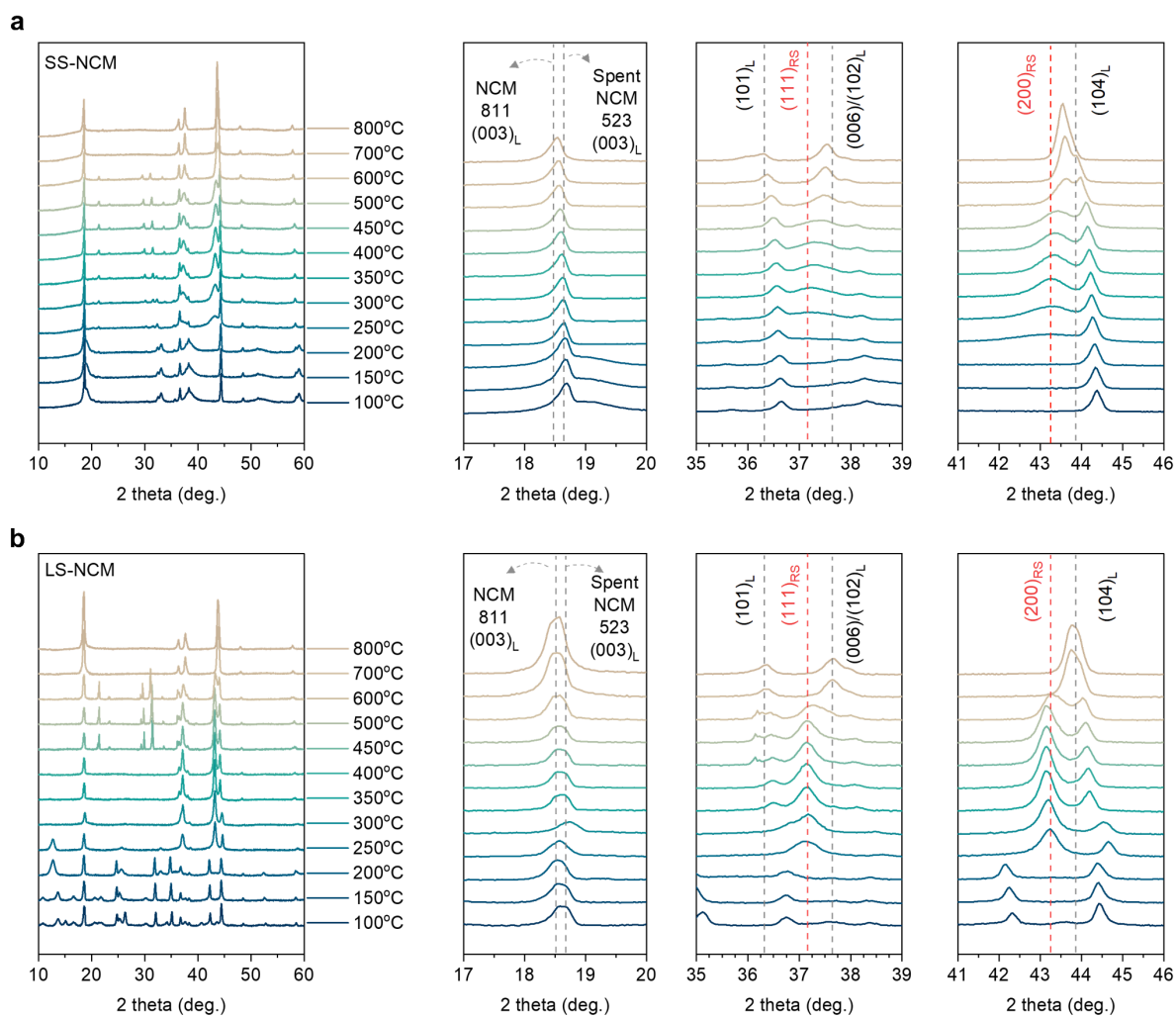


Fig. S11. (a) High-temperature X-ray diffraction (HT-XRD) patterns of the mixture of spent NCM523, LiOH, and Ni(OH)₂ for SS-NCM synthesis. (b) HT-XRD patterns of the mixture of spent NCM523 with a eutectic mixture of LiOH–LiNO₃ and extra Ni(NO₃)₂ for LS-NCM synthesis.

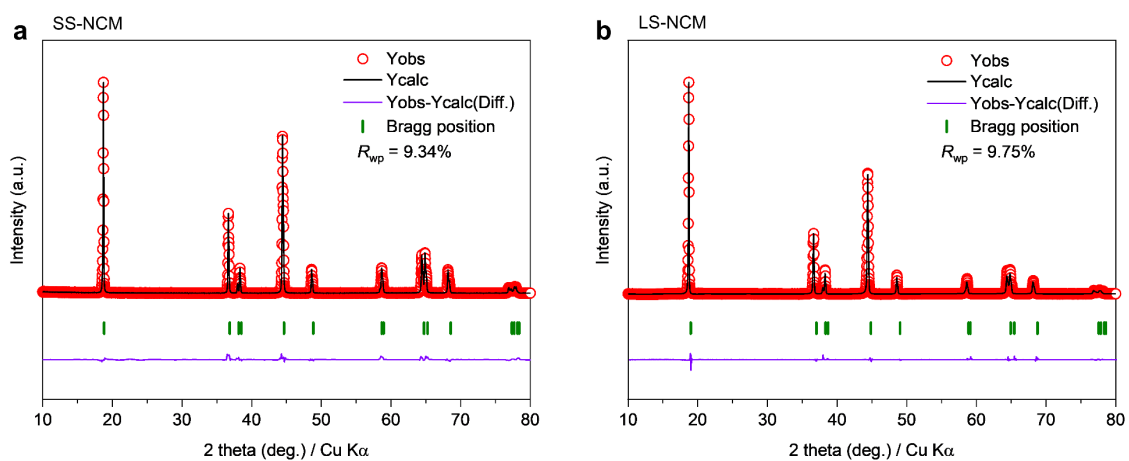


Fig. S12. Rietveld refinement of XRD patterns for (a) SS-NCM and (b) LS-NCM. Fitting details available in Table S3.

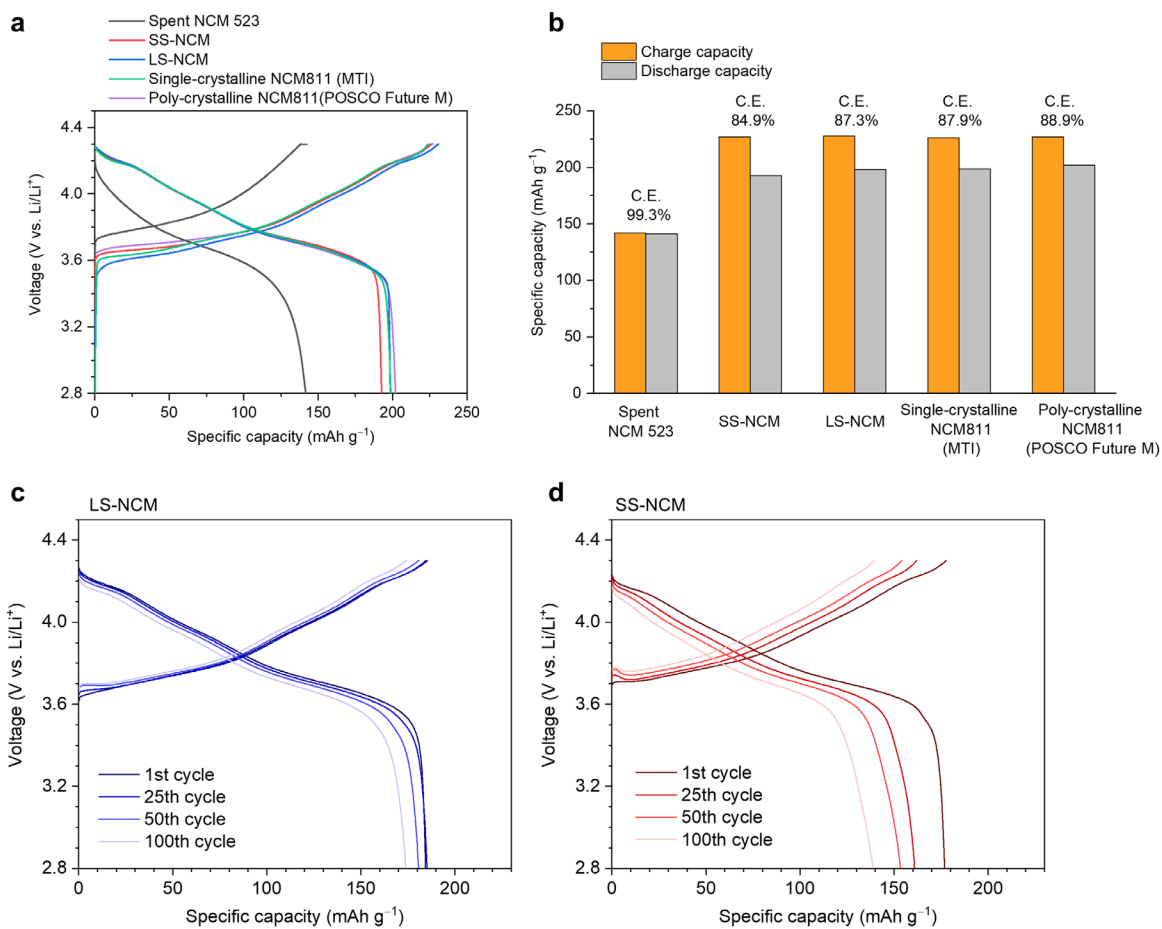


Fig. S13. (a) Charge-discharge voltage profiles of different NCM cathodes, including spent NCM523, SS-NCM, LS-NCM, single-crystalline NCM811 (MTI), and poly-crystalline NCM811 (POSCO Future M), and (b) their corresponding initial coulombic efficiency (C.E.) during the first cycle with 0.1 C charge – 0.1 C discharge within the voltage range of 2.8 – 4.3 V (vs. Li/Li⁺). Voltage profiles of (c) LS-NCM and (d)SS-NCM during 0.5C charge – 1.0 C discharge cycling test within the voltage range of 2.8 – 4.3 V (vs. Li/Li⁺) for 100 cycles at 25°C (1C = 200mA g⁻¹)

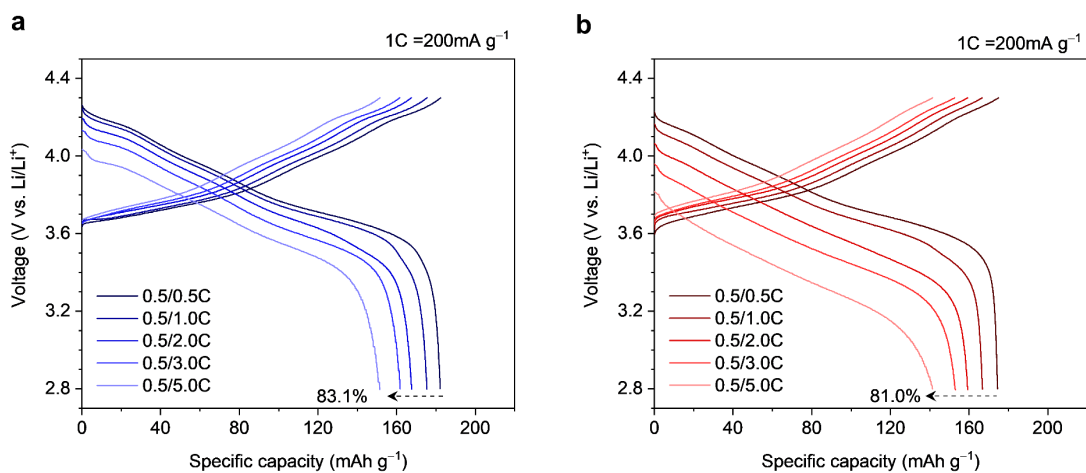


Fig. S14. Charge-discharge curves of (a) LS-NCM and (b)SS-NCM during rate capability test within the voltage range of 2.8 to 4.3 V (vs. Li/Li⁺) at 25°C. The discharge C-rate increased from 0.5 to 5.0 C with a fixed charge C-rate of 0.5 C (1 C = 200mA g⁻¹).

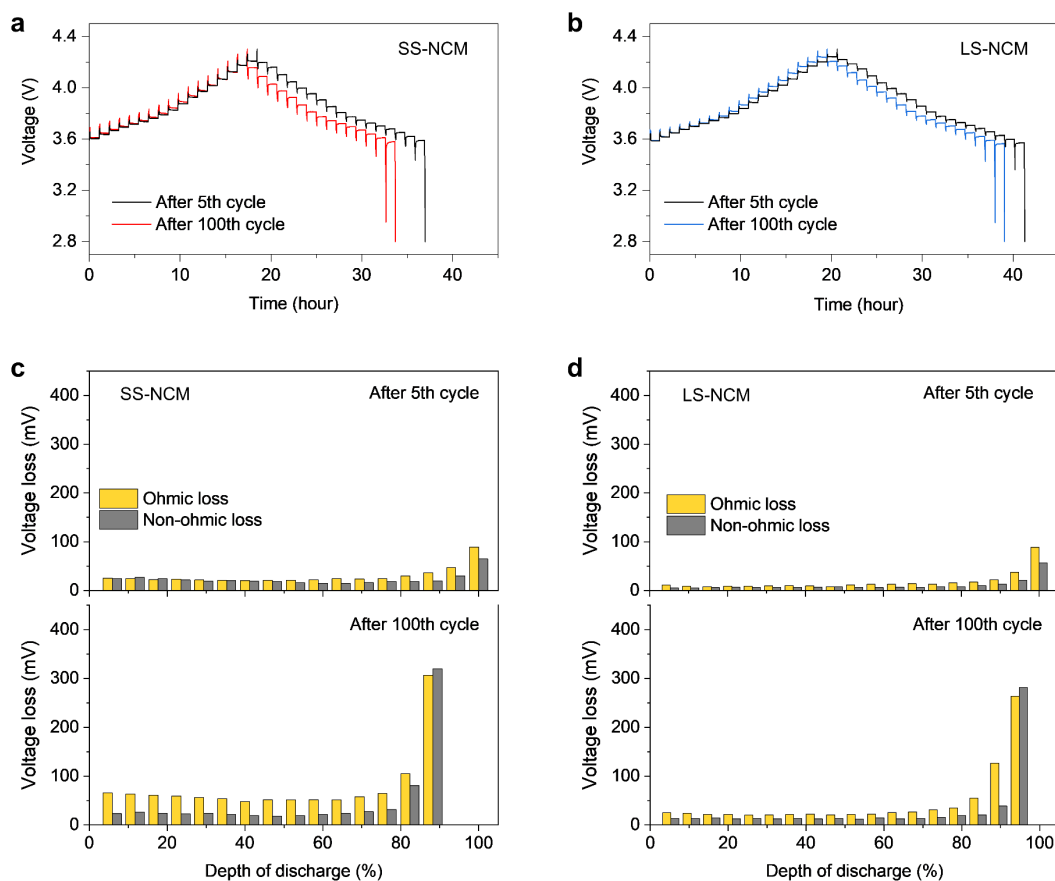


Fig. S15. Galvanostatic intermittent titration technique (GITT) measurements on SS-NCM and LS-NCM after certain cycles during 0.5C/1 C cycling in Fig. 5(d). The voltage profiles after 5th cycle and 100th cycle for (a) SS-NCM and (b) LS-NCM. The ohmic and non-ohmic voltage losses were separately plotted as a function of depth of discharge in (c) SS-NCM and (d) LS-NCM.

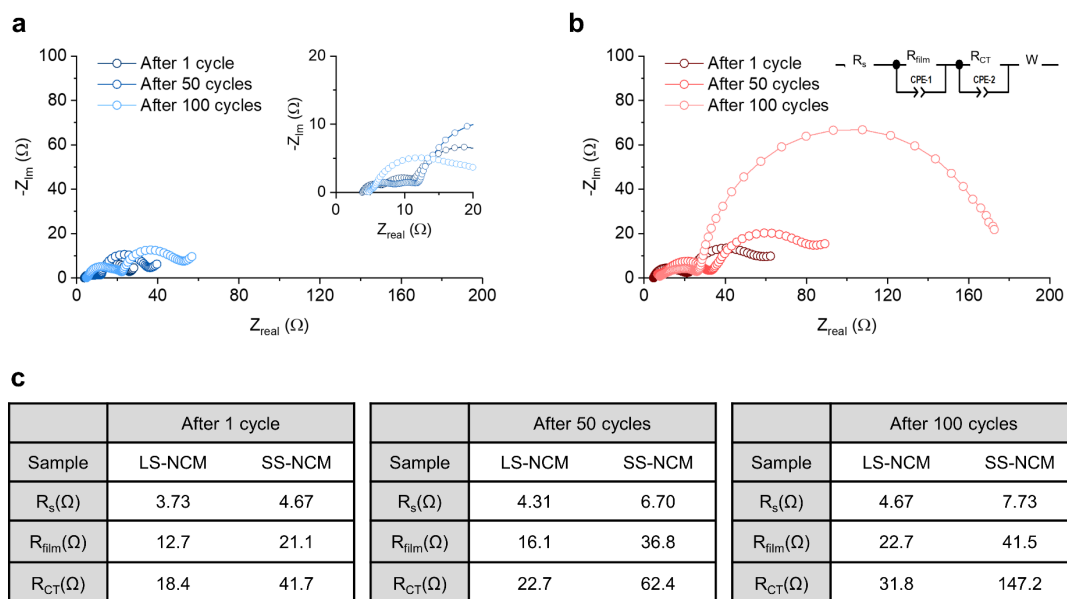


Fig. S16. Electrochemical impedance spectroscopy (EIS) measurements on (a) LS-NCM and (b) SS-NCM after 1, 50 and 100 cycles of 0.5C/1C cycling between 2.8 V and 4.3 V (vs. Li/Li⁺) at 25 °C. Insets: Magnified EIS data and equivalent circuit. Fitted results are listed in (c). R_{CT} contributes most to the impedance of cycled cathodes.

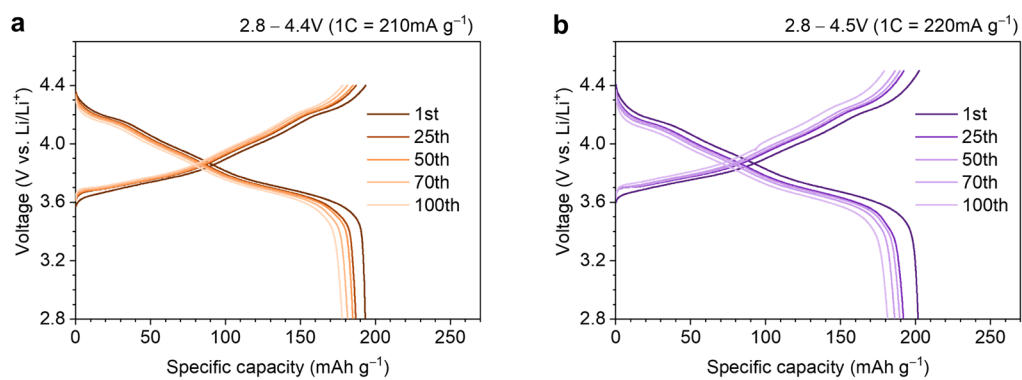


Fig. S17. Voltage profiles of LS-NCM during 0.5C/1.0C cycling test within the voltage range of 2.8 to 4.4 V (vs. Li/Li⁺) for (a) and 2.8 to 4.5 V (vs. Li/Li⁺) for (b) at 25°C.

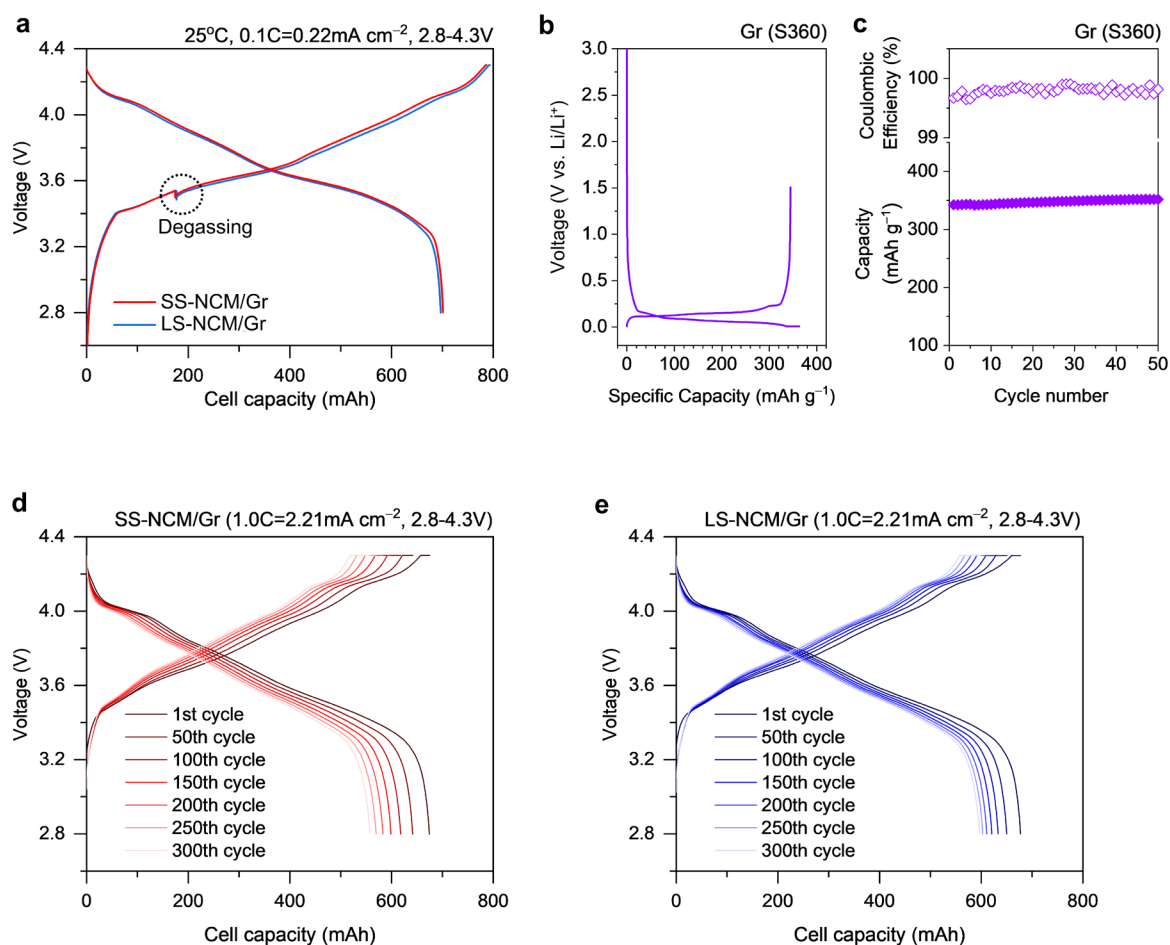


Fig. S18. Electrochemical performance of SS-NCM/spherical graphite (SS-NCM/Gr) and LS-NCM/Gr full-cells tested in the voltage range of 2.8–4.3V at 25°C. (a) Initial full-cell formation step performed at 2.8–4.3 V with a charge and discharge C-rate of 0.1 C. (b) Initial charge-discharge voltage profile of the Gr anode at 25°C (CC-CV mode, charge and discharge C-rate: 0.1 and 0.1C). (c) Cycle performance of the Gr anode at the voltage range of 0.005–1.5 V (vs. Li/Li⁺) with charge and discharge C-rate of 0.5 and 0.5C, respectively. Voltage profiles of (d) SS-NCM/Gr and (e) LS-NCM/Gr full-cells during 300 cycles (galvanostatic charge-discharge cycling was performed with C-rate of 1.0 C \approx 2.21 mA cm⁻²).

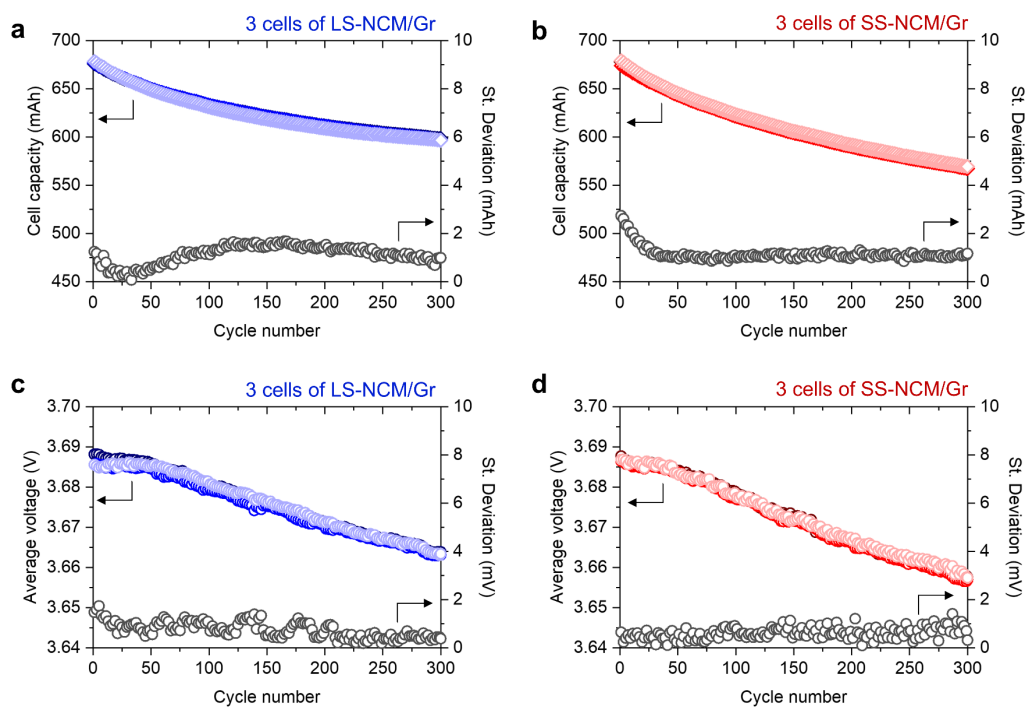


Fig. S19. (a-d) Comparative cycling performance and average voltage retention for three cells of LS-NCM/Gr (left panels, blue) and SS-NCM/Gr (right panels, red) tested up to 300 cycles at 1.0 C in the range of 2.8–4.3 V at 25 °C (galvanostatic charge-discharge cycling was performed with C-rate of 1.0 C \approx 2.21 mA cm^{-2}).

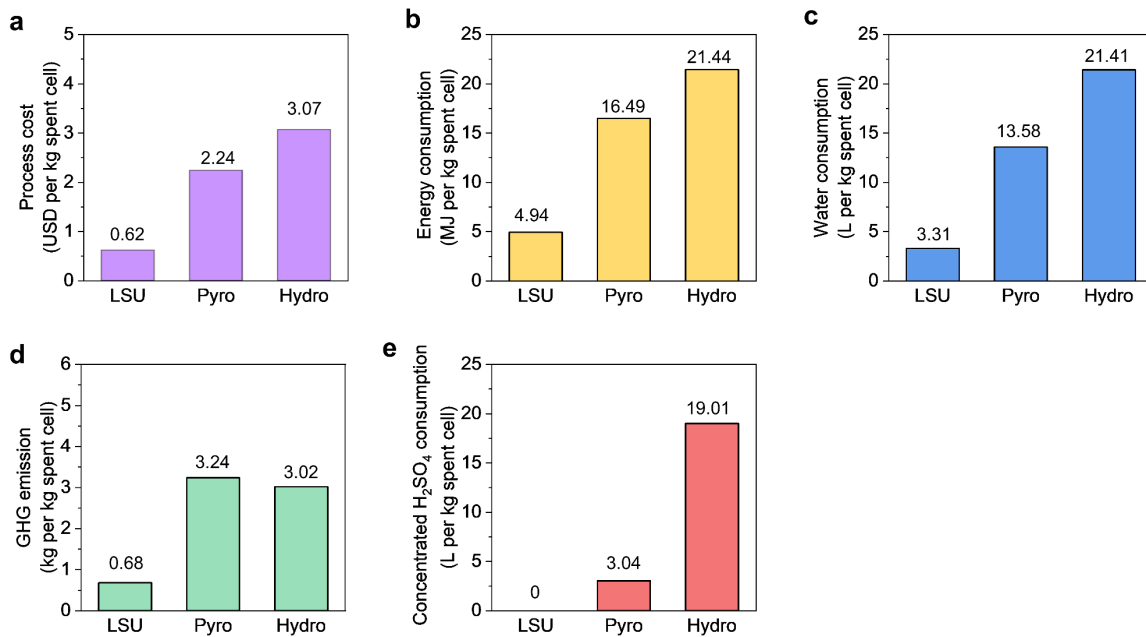


Fig. S20. (a-e) Process cost, energy consumption, water consumption, GHG emission, and concentrated H₂SO₄ consumption in treating 1kg of spent batteries (cells). LSU : liquified-salts-assisted upcycling. Pyro : pyrometallurgical method. Hydro : hydrometallurgical method.

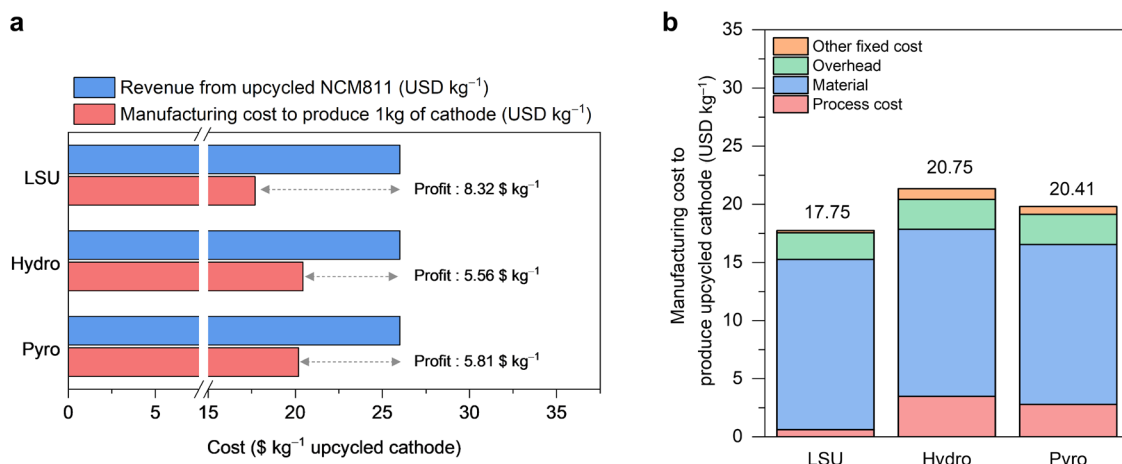


Fig. S21. (a) Manufacturing cost and revenue per kg of NCM811 cathode upcycled by LSU, hydro, and pyro processes. The profits from 1kg of upcycled NCM811 are USD 8.32, 5.56, and 5.81 for LSU, hydro, and pyro methods, respectively. (b) Detailed breakdown of manufacturing costs to produce 1kg of upcycled NCM811 cathode from each process. LSU : liquified-salts-assisted upcycling. Pyro : pyrometallurgical method. Hydro : hydrometallurgical method.

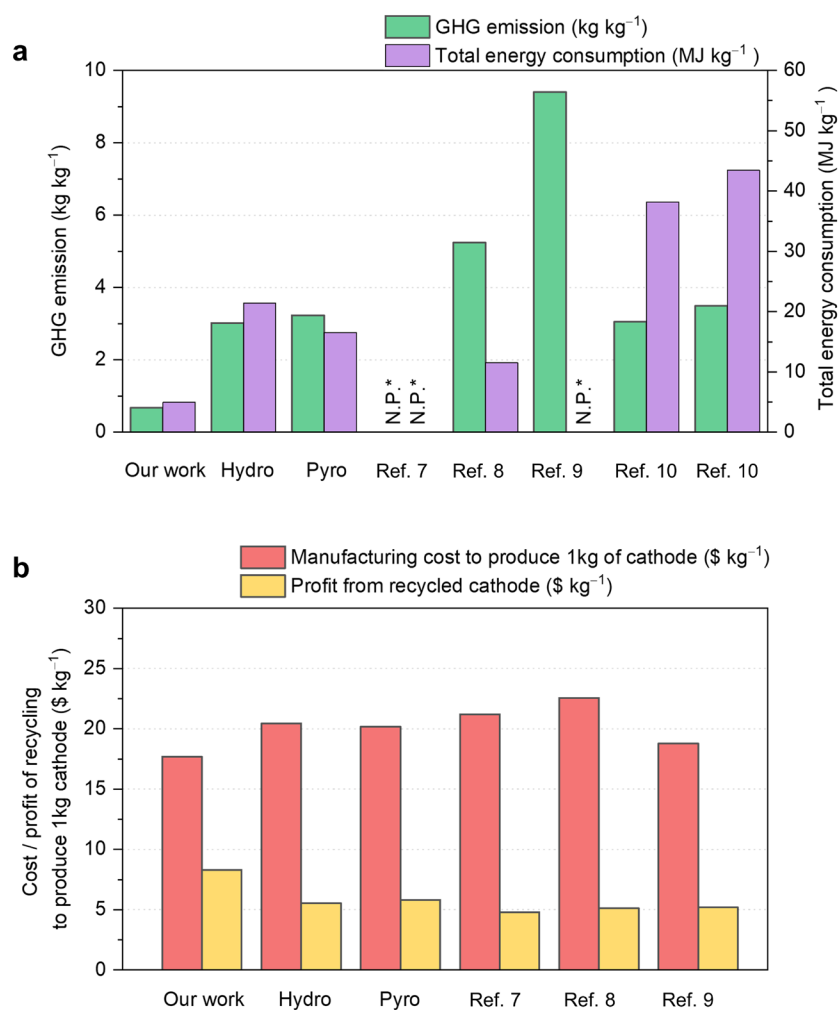


Fig. S22. (a) Estimated GHG emissions and total energy consumption of liquified-salts-assisted upcycling process for recycling 1 kg of spent battery cells. The results are compared with those from other direct upcycling/recycling methods in the literatures. (b) Estimated manufacturing costs and profits of liquified-salts-assisted upcycling process for 1 kg of upcycled NCM811 cathode, compared with other direct upcycling/recycling methods from the literatures. (N.P.* indicates non-provided value from literature).

Table S1. Chemical composition of spent NCM523, LS-NCM and SS-NCM measured by Inductively Coupled Plasma Optical Emission Spectrometry (ICP-OES)

Sample	Mole ratio over (Ni+Co+Mn) (%)				Weight percentage (mg g ⁻¹)	
	Li	Ni	Co	Mn	Al	Cu
Spent NCM523	81.1	49.8	19.2	31.0	/	/
LS-NCM	101.4	80.4	7.99	12.05	/	/
SS-NCM	102.1	80.5	7.68	12.32	/	/

Table S2. Particle size distributions of LS-NCM and SS-NCM.

Sample	BET surface area ($\text{m}^2 \text{g}^{-1}$)	Particle size distribution		
		D_{10} (μm)	D_{50} (μm)	D_{90} (μm)
LS-NCM	0.7811	2.6	5.8	10.2
SS-NCM	1.0776	4.7	8.6	14.3

Table S3. Refined XRD data for LS-NCM and SS-NCM assuming Ni can cation-mixed with Li.

LS-NCM	Element	Site	<i>x</i>	<i>y</i>	<i>z</i>	Occupancy
<i>a</i> =2.874184(3) Å <i>c</i> =14.29982(5) Å <i>R</i> _{wp} = 9.75% <i>R</i> _p = 6.57% Bragg peak ICSD ID : 162291	Li	3a	0	0	0	0.981(6)
	Li	3b	0	0	0.5	<u>0.019(6)</u>
	Co	3b	0	0	0.5	0.082(4)
	Ni	3b	0	0	0.5	0.783(3)
	Mn	3b	0	0	0.5	0.110(6)
	Ni	3a	0	0	0	<u>0.019(6)</u>
	O	6c	0	0	0.259152	1.0(4)
SS-NCM	Element	Site	<i>x</i>	<i>y</i>	<i>z</i>	Occupancy
<i>a</i> =2.85320(3) Å <i>c</i> =14.3420(6) Å <i>R</i> _{wp} = 9.34% <i>R</i> _p = 5.96% Bragg peak ICSD ID : 162291	Li	3a	0	0	0	0.966(6)
	Li	3b	0	0	0.5	<u>0.034(6)</u>
	Co	3b	0	0	0.5	0.083(4)
	Ni	3b	0	0	0.5	0.771(4)
	Mn	3b	0	0	0.5	0.112(4)
	Ni	3a	0	0	0	<u>0.034(6)</u>
	O	6c	0	0	0.241844	1.0(4)

Table S4. Comparison of fresh and upcycled (recycled) Ni-rich cathode materials on the synthesis method, particle size, and electrochemical performances. (*AM : Active material)

Active material (Reference number)	Synthesis method	Particle size	Voltage range (vs. Li/Li ⁺)	Discharge capacity @ 1 st cycle (mAh g ⁻¹)	Capacity retention	Electrode loading and *AM ratio in electrode
Li _{1.0} Ni _{0.8} Co _{0.1} Mn _{0.1} O ₂ (Ref. 11)	Commercial	2-3 μm	3.0-4.3V	180	79.6% after 200 cycles (0.1C)	▪ 10 mg cm ⁻² ▪ 80% CAM
Li _{1.0} Ni _{0.8} Co _{0.1} Mn _{0.1} O ₂ (Ref. 12)	CATL (China)	2-3 μm	2.8-4.3V	195	90.9% after 50 cycles (0.2C)	▪ 10 mg cm ⁻² ▪ 80% CAM
Li _{1.0} Ni _{0.8} Co _{0.1} Mn _{0.1} O ₂ (Ref. 13)	Commercial	2-3 μm	3.0-4.3V	192	89.0% after 100 cycles (1.0C)	▪ 26.4 mg cm ⁻² ▪ 96% CAM
Li _{1.0} Ni _{0.8} Co _{0.1} Mn _{0.1} O ₂ (Ref. 14)	Co-precipitation High-temperature synthesis	2-3 μm	2.7-4.3V	186	85.0% after 100 cycles (0.5C)	▪ 4-5 mg cm ⁻² ▪ 90% CAM
Li _{1.0} Ni _{0.8} Co _{0.1} Mn _{0.1} O ₂ (Ref. 15)	Commercial	3-6 μm	2.8-4.3V	184	86.5% after 200 cycles (1.0C)	▪ 3.75 mg cm ⁻² ▪ 80% CAM
Li _{1.0} Ni _{0.88} Co _{0.09} Al _{0.03} O ₂ (Ref. 16)	Co-precipitation High-temperature synthesis	3-6 μm	3.0-4.3V	185	85.0% after 100 cycles (0.2C)	▪ 12 mg cm ⁻² ▪ 92% CAM
Li _{1.0} Ni _{0.8} Co _{0.1} Mn _{0.1} O ₂ (Ref. 17)	Commercial	~3 μm	3.0-4.3V	180	77.4% after 200 cycles (0.5C)	▪ 7 mg cm ⁻² ▪ 90% CAM
Li _{1.0} Ni _{0.83} Co _{0.11} Mn _{0.06} O ₂ (Ref. 18)	Co-precipitation High-temperature synthesis	1-4 μm	2.75-4.4V	191	84.5% after 150 cycles (1.0C)	▪ 8.5 mg cm ⁻² ▪ 89% CAM
Li _{1.0} Ni _{0.8} Co _{0.1} Mn _{0.1} O ₂ (Ref. 19)	Co-precipitation High-temperature synthesis	2-3 μm	2.5-4.4V	210	92.6% after 100 cycles (0.33C)	▪ 3 mg cm ⁻² ▪ 80% CAM
Li _{1.0} Ni _{0.8} Co _{0.1} Mn _{0.1} O ₂ (Ref. 20)	Co-precipitation High-temperature synthesis	2-5 μm	2.8-4.5V	190	58.7% after 400 cycles (1.0C)	▪ 4 mg cm ⁻² ▪ 80% CAM
LiNi _{0.8} Mn _{0.12} Co _{0.08} O ₂ (Ref. 7)	Direct upcycling	1-2 μm	2.8-4.3V	175	85.0% after 200 cycles (1.0C)	▪ 2-3 mg cm ⁻² ▪ 90% CAM
Li _{1.13} Ni _{0.88} Co _{0.095} Al _{0.025} O ₂ (Ref. 21)	Direct upcycling	1-2 μm	3.0-4.3V	200	93.3% after 100 cycles (1.0C)	▪ 15 mg cm ⁻² ▪ 90% CAM
Li _{1.0} Ni _{0.8} Co _{0.1} Mn _{0.1} O ₂ (Ref. 22)	Direct upcycling	~1 μm	2.7-4.3V	192	88.7% after 100 cycles (0.2C)	▪ 3 mg cm ⁻² ▪ 80% CAM
Li _{1.0} Ni _{0.8} Co _{0.1} Mn _{0.1} O ₂ (Ref. 23)	Direct regeneration	12~10 μm	3.0-4.3V	198	85.5 % after 50 cycles (0.5C)	▪ 4 mg cm ⁻² ▪ 80% CAM
Li _{1.0} Ni _{0.8} Co _{0.1} Mn _{0.1} O ₂ (Ref. 24)	Direct regeneration	8~10 μm	2.7-4.3V	155	63.5 % after 300 cycles (3.0C)	▪ Unknown ▪ 90% CAM
Our work	Liquified-salts- assisted upcycling	3-5 μm	2.8-4.3V	178	94.1% after 100 cycles (1.0C)	▪ ~12 mg cm ⁻² ▪ 90% CAM
			2.8-4.4V	193	91.7% after 100 cycles (1.0C)	▪ ~12 mg cm ⁻² ▪ 90% CAM
			2.8-4.5V	201	90.4% after 100 cycles (1.0C)	▪ ~12 mg cm ⁻² ▪ 90% CAM

Table S5. Full-cell specifications. (CC: constant current. CV: constant voltage.)

Full-cell specifications		
Electrodes	Cathode	Anode
Materials	LS-NCM / SS-NCM	Spherical graphite (Gr)
Cell dimension	72.5 mm*55 mm	75.5 mm*58mm
Composition	Active material (AM) : CM : Bi = 94 : 3 : 3 (CM: Super P, Bi: polyvinylidene fluoride, PVDF)	AM : CB : CMC : SBR = 97.0 : 0.5 : 1.1 : 1.4 (CB: carbon black, CMC: carboxymethyl cellulose, SBR: styrene butadiene rubber)
One-side Loading level (mg cm ⁻²)	12.04 ± 0.4	6.88 ± 0.4
Two-side Loading level (mg cm ⁻²)	24.10 ± 0.5	13.75 ± 0.5
Electrode thickness (μm)	87 ± 4 (Al foil thickness of 15μm included)	101.5 ± 1 (Cu foil thickness of 10μm included)
Electrode density (g cm ⁻³)	3.31 ± 0.02	1.52 ± 0.02
Stacking	4	5
Negative/positive (N/P) ratio	1.07 ± 0.01	
Separator thickness (μm)	16	
Amount of electrolyte	1.75 g (~2.5g Ah ⁻¹)	
Formation step testing condition	Voltage range: 2.8 – 4.3 V Charge: 0.1C (CC) – 0.05C (CV) / Discharge: 0.1C (CC) Charge/discharge current density: 1C≈2.21 mA cm ⁻²	
Cycling test condition	Voltage range: 2.8 – 4.3 V Charge: 1.0C (CC) – 0.05C (CV) / Discharge: 1.0C (CC) Charge/discharge current density: 1C≈2.21 mA cm ⁻²	

Table S6. The gravimetric composition of commercial lithium-ion batteries

Materials	Ratio (wt%)	Materials	Ratio (wt%)
Cathode materials	~33.5	Graphite anode	~21.3
Conductive carbon and Binder	~5.3	Separator	~1.3
Aluminum	~5.3	Copper	~13.3
Electrolyte	~14.7	Others	~5.3

Table S7. Life cycle inventory of pyrometallurgy upcycling method.

Pyrometallurgy upcycling method					
Procedures	Input	Amount	Output	Amount	Notes
Discharging and collecting	Spent batteries	1.00 kg	Spent batteries (100% SOD)	1.00 kg	The data is estimated based on Everbatt 2020. 1 MJ electricity produces 0.12 kg GHG and consumes 0.53 L water. 1 kg of U.S. conventional diesel produces 37.9 MJ energy. ~5 wt% NaCl solution is used for the discharging process. [Ref. 3]
	Energy	0.03 MJ	GHG	0.004 kg	
	Water	0.52 L	/	/	
Smelting + Gas treatment + Water-leaching	Spent batteries (100% SOD)	1.00 kg	Matte (Co, Ni, Mn, Cu)	0.338 kg	The purpose is to reduce the transition metals and remove all the impurities. The temperature is ~1873 K for 3 h. The byproducts include the slag with Al, Ca, and Li, which requires the post-treatment to recycle the Li salts. The ratio of liquid to solid for water-leaching is set 2:1. [Ref. 25,26]
	Energy	2.42 MJ	GHG	1.569 kg	
	Water	1.81 L	Slag residue (Li ₂ CO ₃ , CaAl)	0.263kg	
	Slag formation reagent	0.22 kg	/	/	
Granulator	Matte (Co, Ni, Mn, Cu)	1.00 kg	Fine metal particles	1.00 kg	[Ref. 26]
	Energy	0.007 MJ	GHG	0.001 kg	
	Water	0.004 L	/	/	
Acid leaching	Fine metal particles	1.00 kg	Leachate	~20 kg	The average pulp density is ~5% and the concentration is ~1.47 M H ₂ SO ₄ for the pyrometallurgical method. The density of 10 M H ₂ SO ₄ is ~1.54 g cm ⁻³ . [Ref. 27]
	Energy	0.11 MJ	GHG	0.013 kg	
	Water	11.4 L	Cu compounds	0.41 kg	
	10 M H ₂ SO ₄ solution	3.04 kg	/	/	
	NiSO ₄ · 6H ₂ O	4.56 kg	/	/	

Co-precipitation	Leachate	1.00 kg	Transition metal hydroxide	0.108 kg	The pH is adjusted to 10-11. The details to adjust the pH to precipitate hydroxide precursor is omitted here for the convenience of calculation since the amount of reagent (NH ₄ OH) is too small. [Ref. 28]
	Energy	0.61 MJ	GHG	0.07 kg	
	NaOH	0.046 kg	/	/	
	Water	0.32 L	/	/	
High-temperature resynthesize	Transition metal hydroxide	1.00 kg	Resynthesized cathode	1.10 kg	The molar ratio of Li: TM=1.03 and the mixture is calcined at 723 K for 5 h and 1123 K for 14 h. [Ref. 28]
	LiOH·H ₂ O	0.466 kg	GHG	1.62 kg	
	Energy	13.53 MJ	/	/	
	Water	7.17 L	/	/	

Table S8. Life cycle inventory of hydrometallurgy upcycling method.

Hydrometallurgy upcycling method					
Procedures	Input	Amount	Output	Amount	Notes
Discharging and collecting	Spent batteries	1.00 kg	Spent batteries (100% SOD)	1.00 kg	The data is estimated based on Everbatt 2020. 1 MJ electricity produces 0.12 kg GHG and consumes 0.53 L water. 1 kg of U.S. conventional diesel produces 37.9 MJ energy. ~5 wt% NaCl solution is used for the discharging process. [Ref. 3]
	Energy	0.03 MJ	GHG	0.004 kg	
	Water	0.52 L	/	/	
Shredding	Spent batteries (100% SOD)	1.00 kg	Battery pieces	0.81 kg	The battery pieces included the spent batteries without the organic solvents. Recycling rate in shredding process is set to 95%. [Ref. 26]
	Energy	0.38 MJ	GHG	0.046 kg	
	Water	0.20 L	Electrolyte	0.14 kg	
Incineration + Sieving	Battery pieces	1.00 kg	Black mass	0.642 kg	The purpose is to separate the active materials with current collectors, to decompose the binder, electrolyte residue, plastics, and SEI. The temperature is ~873 K for 2 h. [Ref. 29]
	Energy	0.31 MJ	GHG	0.626 kg	
	Water	0.16 L	Current collector	0.218 kg	
Wet granulation	Black mass	1.00 kg	Granulated particles	0.99 kg	The amount of water is set to ~20 wt% of the solid. Recycling rate in wet granulation is set to 99%. [Ref. 30]
	Energy	0.007 MJ	GHG	0.001 kg	
	Water	0.204 L	/	/	
Froth flotation	Spent active materials	1.00 kg	Spent cathode powder	0.61 kg	The purpose is to separate the anode materials. [Ref. 26]
	Energy	0.67 MJ	GHG	0.087 kg	
	Water	3.36 L	Spent graphite	0.39 kg	

Acid leaching	Spent cathode powder	1.00 kg	Leachate	~50 kg	The average pulp density is ~2% and the concentration is ~3.27 M H ₂ SO ₄ for the hydrometallurgy method. The density of 10 M H ₂ SO ₄ is ~1.54 g cm ⁻³ . [Ref. 31]
	Energy	0.11 MJ	GHG	0.065 kg	
	Water	25.37 L	/	/	
	10 M H ₂ SO ₄ solution	19.01 kg	/	/	
	NiSO ₄ · 6H ₂ O	4.62 kg	/	/	
Co- precipitation	Leachate	1.00 kg	Transition metal hydroxide	0.051 kg	The pH is adjusted to 10-11. The details to adjust the pH to precipitate hydroxide precursor is omitted here for the convenience of calculation since the amount of reagent (such as NH ₄ OH) is too small. [Ref. 28]
	Energy	0.61MJ	Li ₂ CO ₃	0.008 kg	
	NaOH	0.022 kg	GHG	0.07 kg	
	Na ₂ CO ₃	0.010 kg	/	/	
	Water	0.32 L	/	/	
High-temperature resynthesize	Transition metal hydroxide	1.00 kg	Resynthesized cathode	1.10 kg	The molar ratio of Li: TM=1.03 and the mixture is calcined at 723 K for 5 h and 1123 K for 14 h. [Ref. 28]
	LiOH·H ₂ O	0.466 kg	GHG	1.62 kg	
	Energy	13.53 MJ	/	/	
	Water	7.17 L	/	/	

Table S9. Life cycle inventory of liquified-salts-assisted upcycling method.

Liquified-salts-assisted upcycling method					
Procedures	Input	Amount	Output	Amount	Notes
Discharge + collecting	Spent batteries	1.00 kg	Spent batteries (100% SOD)	1.00 kg	1 MJ electricity produces 0.13 kg GHG and 0.67 L water. 1 kg diesel produces 45.6 MJ energy. The data is estimated based on Everbatt 2020. ~5 wt% NaCl solution is used for the discharging process. [Ref. 3]
	Energy	0.03 MJ	GHG	0.004 kg	
	Water	0.52 L	/	/	
Disassembly + Low-temperature calcination + Scrapping	Spent batteries (100% SOD)	1.00 kg	Cathode material	0.34 kg	The purpose of low-temperature calcination is to decompose the binder, electrolyte residue, and SEI. The temperature is ~623 K for 10min. Manual disassembly is considered to separate the spent active materials. The dismantling step can be achieved by a commercial core drill with a silicon carbide blade, which can reduce the manual disassembly cost. [Ref. 7, 32, 33]
	Energy	0.40 MJ	Al foil	0.05 kg	
	Water	0.21 L	Anode electrode	0.37 kg	
	/	/	Electrolyte	0.15 kg	
	/	/	Separator and others	0.07 kg	
	/	/	GHG	0.090 kg	
Planetary centrifugal mixing + High- temperature resynthesize	Spent cathode powder	0.34 kg	Upcycled cathode	1.0 kg	Conduct planetary centrifugal mixing for 15min on the powder mixture to form homogeneous liquified mixture of spent cathode powder and molten-salts. The energy requirement for planetary centrifugal mixer is 1.33MJ kg ⁻¹ . Then, the powder mixture is calcined at 1193 K for 2 h and subsequently at 1053K for 8h.
	LiOH·H ₂ O	0.120 kg	GHG	1.73 kg	
	LiNO ₃ ·H ₂ O	0.296 kg	/	/	
	Ni(NO ₃) ₂ ·6H ₂ O	1.630 kg	/	/	
	Energy	14.33 MJ	/	/	
	Water	7.59 L	/	/	

Table S10. Required resources and products for upcycling of spent battery

	Cost (unit)	Requirements for upcycling 1kg of spent battery			Ref.
		Pyro	Hydro	LSI	
Energy	0.111 (USD MJ ⁻¹)	16.49 MJ	21.44 MJ	4.94 MJ	Ref. 26
Water	0.018 (USD L ⁻¹)	13.58 L	21.41 L	3.31 L	Ref. 26
Wastewater Treatment	0.027 (USD L ⁻¹)	5.84 L	10.74 L	0.36 L	Ref. 26
Spent batteries (with NCM523)	3.2 (USD kg ⁻¹)	1 kg	1 kg	1 kg	Ref. 34
Concentrated H ₂ SO ₄	0.12 (USD L ⁻¹)	1.03 L	5.97 L	/	Ref. 26
NiSO ₄ · 6H ₂ O	3.2 (USD kg ⁻¹)	1.54 kg	1.45 kg	/	Ref. 26 Ref. 35
Ni(NO ₃) ₂ · 6H ₂ O	3.82 (USD kg ⁻¹)	/	/	1.63 kg	Ref. 26 Ref. 35
LiOH · H ₂ O	9.50 (USD kg ⁻¹)	0.34 kg	0.37 kg	0.12 kg	Ref. 26 Ref. 36
LiNO ₃ · H ₂ O	13.78 (USD kg ⁻¹)	/	/	0.296 kg	Ref. 26 Ref. 36
Total cost in upcycling 1kg of spent batteries	(USD kg cell ⁻¹)	\$ 13.73	\$ 15.17	\$ 15.27	Ref. 26
Products of upcycling process from medium-Ni to Ni-rich cathode					
Amount of upcycled NCM811 Cathode from each process	/	0.8 kg	0.88 kg	1.00 kg	Ref. 26
Total manufacturing cost to produce 1kg of upcycled NCM811	26.0 (USD kg ⁻¹)	\$ 20.41	\$ 20.75	\$ 17.74	Ref. 26

Supplementary References

1. J. Yu, J. Li, S. Zhang, F. Wei, Y. Liu and J. Li, *Proceedings of the National Academy of Sciences*, 2023, **120**, e2217698120.
2. P. Xu, Q. Dai, H. Gao, H. Liu, M. Zhang, M. Li, Y. Chen, K. An, Y. S. Meng, P. Liu, Y. Li, J. S. Spangenberg, L. Gaines, J. Lu and Z. Chen, *Joule*, 2020, **4**, 2609-2626.
3. M. Wang, A. Elgowainy, U. Lee, A. Bafana, P. T. Benavides, A. Burnham, H. Cai, Q. Dai, U. R. Gracida-Alvarez, T. R. Hawkins, P. V. Jaquez, J. C. Kelly, H. Kwon, Z. Lu, X. Liu, L. Ou, P. Sun, O. Winjobi, H. Xu, E. Yoo, G. G. Zaires and G. Zang, *Summary of Expansions and Updates in GREET® 2020*, U.S. Department of Energy, Office of Scientific and Technical Information, Lemont, IL, USA, 2020.
4. N. Li, J. Guo, Z. Chang, H. Dang, X. Zhao, S. Ali, W. Li, H. Zhou and C. Sun, *RSC Advances*, 2019, **9**, 23908-23915.
5. J. Wang, J. Ma, Z. Zhuang, Z. Liang, K. Jia, G. Ji, G. Zhou and H.-M. Cheng, *Chem. Rev.*, 2024, **124**, 2839-2887.
6. C. W. Bale, E. BÉlisle, P. Chartrand, S. A. Deckerov, G. Eriksson, A. E. Gheribi, et al., *Calphad*, 2016, **54**, 35-53.
7. G. Qian, Z. Li, Y. Wang, X. Xie, Y. He, J. Li, Y. Zhu, S. Xie, Z. Cheng, H. Che, Y. Shen, L. Chen, X. Huang, P. Pianetta, Z.-F. Ma, Y. Liu and L. Li, *Cell Reports Physical Science*, 2022, **3**.
8. Wang, J., Ji, H., Li, J. *et al.* Direct recycling of spent cathode material at ambient conditions via spontaneous lithiation. *Nat Sustain.*, 2024, **7**, 1283–1293
9. Zhao, P. et al. Urea solvothermal regeneration of spent $\text{LiNi}_{0.5}\text{Co}_{0.2}\text{Mn}_{0.3}\text{O}_2$: Performance and environmental benefits. *Sep. Purif. Technol.*, 2025, **357**, 129988
10. Fan, M. *et al.* Reviving Fatigue Surface for Solid-State Upcycling of Highly Degraded Polycrystalline $\text{LiNi}_{1-x-y}\text{Co}_x\text{Mn}_y\text{O}_2$ Cathodes. *Adv. Mater.*, 2024, **36**, 2405238
11. X. Kong, Y. Zhang, S. Peng, J. Zeng and J. Zhao, *ACS Sustain. Chem. Eng.*, 2020, **8**, 14938-14948.
12. C.-G. Shi, X. Peng, P. Dai, P. Xiao, W.-C. Zheng, H.-Y. Li, H. Li, S. Indris, S. Mangold, Y.-H. Hong, C.-X. Luo, C.-H. Shen, Y.-M. Wei, L. Huang and S.-G. Sun, *Adv. Energy Mater.*, 2022, **12**, 2200569.
13. H. Cha, J. Kim, H. Lee, N. Kim, J. Hwang, J. Sung, M. Yoon, K. Kim and J. Cho, *Adv. Mater.*, 2020, **32**, 2003040.
14. H.-H. Ryu, B. Namkoong, J.-H. Kim, I. Belharouak, C. S. Yoon and Y.-K. Sun, *ACS Energy Lett.*, 2021, **6**, 2726-2734.
15. X. Chen, Y. Tang, C. Fan and S. Han, *Electrochim. Acta*, 2020, **341**, 136075.
16. H. Li, J. Li, N. Zaker, N. Zhang, G. A. Botton and J. R. Dahn, *J. Electrochem. Soc.*, 2019, **166**, A1956.
17. Y.-G. Zou, F. Meng, D. Xiao, H. Sheng, W.-P. Chen, X.-H. Meng, Y.-H. Du, L. Gu, J.-L. Shi and Y.-G. Guo, *Nano Energy*, 2021, **87**, 106172.
18. X. Fan, G. Hu, B. Zhang, X. Ou, J. Zhang, W. Zhao, H. Jia, L. Zou, P. Li and Y. Yang, *Nano Energy*, 2020, **70**, 104450.
19. R. Zhang, C. Wang, M. Ge and H. L. Xin, *Nano Lett.*, 2022, **22**, 3818-3824.
20. M. Liu, J. Zhou, T. Cheng, Z. Feng, Y. Qin and B. Guo, *ACS Appl. Energy Mater.*, 2022, **5**, 9181-9188.

21. Z. Qin, Y. Zhang, W. Luo, T. Zhang, T. Wang, L. Ni, H. Wang, N. Zhang, X. Liu, J. Zhou and G. Chen, *Angew. Chem. Int. Ed.*, 2023, **62**, e202218672.
22. K. S. Kim, M. K. Jeon, S. H. Song, S. Hong, H. S. Kim, S.-W. Kim, J. Kim, P. Oh, J. Hwang, J. Song, J. Ma, J.-J. Woo, S.-H. Yu and H. Kim, *Journal of Materials Chemistry A*, 2023, **11**, 21222-21230.
23. Z. Feng, S. Zhang, X. Huang, Y. Ren, D. Sun, Y. Tang, Q. Yan and H. Wang, *Small*, 2022, **18**, 2107346.
24. S. Ko, J. Choi, J. Hong, C. Kim, U. Hwang, M. Kwon, G. Lim, S. S. Sohn, J. Jang, U. Lee, C. B. Park and M. Lee, *Energy Environ. Sci.*, 2024, **17**, 4064-4077.
25. C. Peng, F. Liu, Z. Wang, B. P. Wilson and M. Lundström, *J. Power Sources*, 2019, **415**, 179-188.
26. Q. Dai, J. Spangenberg, S. Ahmed, L. Gaines, J. C. Kelly and M. Wang, *EverBatt: A Closed-loop Battery Recycling Cost and Environmental Impacts Model*, 2019.
27. J. Xiao, J. Li and Z. Xu, *Environ. Sci. Technol.*, 2017, **51**, 11960-11966.
28. X. Ma, M. Chen, Z. Zheng, D. Bullen, J. Wang, C. Harrison, E. Gratz, Y. Lin, Z. Yang, Y. Zhang, F. Wang, D. Robertson, S.-B. Son, I. Bloom, J. Wen, M. Ge, X. Xiao, W.-K. Lee, M. Tang, Q. Wang, J. Fu, Y. Zhang, B. C. Sousa, R. Arsenaault, P. Karlson, N. Simon and Y. Wang, *Joule*, 2021, **5**, 2955-2970.
29. Y. Zheng, S. Wang, Y. Gao, T. Yang, Q. Zhou, W. Song, C. Zeng, H. Wu, C. Feng and J. Liu, *ACS Appl. Energy Mater.*, 2019, **2**, 6952-6959.
30. A. Miwa, T. Yajima and S. Itai, *Int. J. Pharm.*, 2000, **195**, 81-92.
31. P. Zhang, T. Yokoyama, O. Itabashi, T. M. Suzuki and K. Inoue, *Hydrometallurgy*, 1998, **47**, 259-271.
32. M. Sethurajan and S. Gaydardzhiev, *Resources, Conservation and Recycling*, 2021, **165**, 105225.
33. W. Chen, Y. Cheng, J. Chen, K. V. Bets, R. V. Salvatierra, C. Ge, J. T. Li, D. X. Luong, C. Kittrell, Z. Wang, E. A. McHugh, G. Gao, B. Deng, Y. Han, B. I. Yakobson and J. M. Tour, *Nat. Commun.*, 2024, **15**, 6250.
34. Lithium-Ion Battery Scrap Prices in the U.S.A.. (accessed 18 November 2024) <https://www.scrapmonster.com/scrap-yard/price/lithium-ion-battery-scrap/122>
35. Nickel Sulfate (Battery Grade) Price, USD/mt. (accessed 18 November 2024) <https://www.metal.com/Nickel/201908270001>
36. Lithium Hydroxide (56.5% Battery Grade, Coarse Particle) Price, USD/mt (accessed 18 November 2024) <https://www.metal.com/Lithium/201102250281>